Nano Research

Open Access

Research Article

A cRGD-engineered EV-liposome hybrid nanoplatform for targeted FAT1 mRNA delivery suppresses thyroid carcinoma metastasis by reprogramming the immunosuppressive microenvironment

Wenjuan Wang[1,§], Jian Zhou[2,§], Baorui Tao[2,§], Ning Kong[3]✉, and Jie Shao[2]✉

[1] *Department of Pathology, Huashan Hospital, Fudan University, Shanghai 200040, China*
[2] *Department of General Surgery, Huashan Hospital, Fudan University, Shanghai 200040, China*
[3] *Department of Rheumatology and Immunology, Huashan Hospital, Fudan University, Shanghai 200040, China*
[§] *Wenjuan Wang, Jian Zhou, and Baorui Tao contributed equally to this work.*

Cite this article: *Nano Research*, **2026**, *19*, 94908637. https://doi.org/10.26599/NR.2026.94908637

ABSTRACT: This study developed a cRGD-modified mesenchymal stem cell-derived extracellular vesicle-liposome hybrid nanosystem (ELH@FAT1) for targeted delivery of FAT1 mRNA to treat thyroid carcinoma (THCA). Analysis of TCGA datasets revealed that reduced FAT1 expression is significantly associated with poor prognosis in patients with THCA. The engineered ELH@FAT1 nanosystem exhibited excellent stability and delivery efficiency, successfully restoring FAT1 expression in both THCA cells and tumor-associated macrophages (TAMs). Functional experiments revealed that ELH@FAT1 significantly suppressed C-X-C motif chemokine ligand 8 (CXCL8) secretion from M2-type TAMs, thereby disrupting the immune stemness feedback loop between TAMs and tumor stem cells (TSCs). This disruption led to diminished epithelial-mesenchymal transition (EMT), reduced cancer stemness maintenance, and inhibited metastatic capacity. Single-cell RNA sequencing (scRNA-seq) further confirmed the remodeling of the immunosuppressive tumor microenvironment (TME) and interruption of the CXCL8-mediated TAM-TSC crosstalk following ELH@FAT1 treatment. *In vivo* studies demonstrated that ELH@FAT1 effectively inhibited tumor growth and lung metastasis, while CXCL8 compensation or FAT1 silencing abolished these therapeutic effects. This work provides a novel nanotherapeutic strategy targeting the FAT1-CXCL8 axis to reprogram the immunosuppressive microenvironment and inhibit THCA progression.

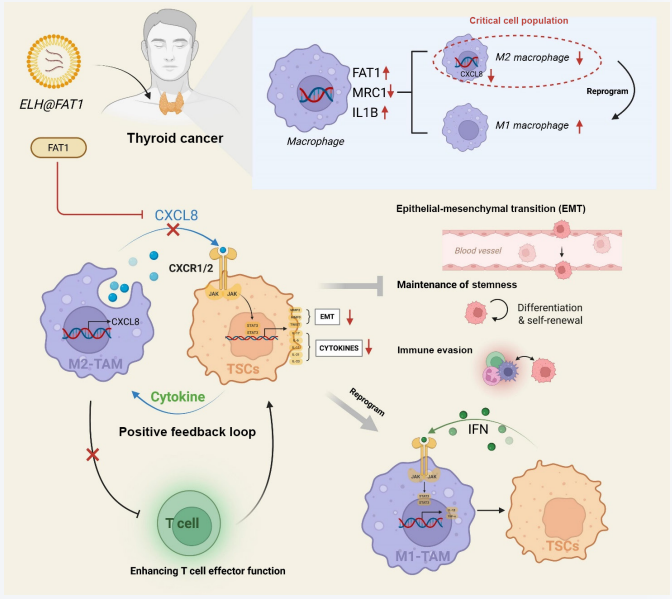

KEYWORDS: FAT1, C-X-C motifchemokine ligand 8 (CXCL8), tumor stemness, tumor-associated macrophages, thyroid carcinoma, nanosystem delivery

1 Introduction

Thyroid carcinoma (THCA) is among the most prevalent malignancies of the endocrine system. Although the majority of patients achieve favorable outcomes following early surgical intervention and radioactive iodine therapy, the prognosis remains poor for individuals with undifferentiated tumors or distant metastases [1, 2]. Notably, in cases characterized by therapeutic resistance, tumor recurrence, and metastatic dissemination, tumor stem cells (TSCs) are regarded as key drivers of malignant progression [3, 4]. TSCs exhibit robust self-renewal and metastatic

Received: August 27, 2025; **Revised:** March 12, 2026
Accepted: March 13, 2026

✉Address correspondence to Ning Kong, nkong@unirheuma.org; Jie Shao, shaojie_hsyy@fudan.edu.cn

potential and play pivotal roles in sustaining tumor heterogeneity, promoting epithelial-mesenchymal transition (EMT), and enabling immune evasion [4, 5]. Accumulating evidence indicates that TSC function is highly dependent on the tumor microenvironment (TME), particularly the regulatory influence exerted by immune cell networks [6]. Within this context, tumor-associated macrophages (TAMs), especially those polarized toward the immunosuppressive M2 phenotype, have been recognized as critical microenvironmental factors supporting TSC stemness [4, 7].

Notably, M2-polarized TAMs secrete the proinflammatory chemokine CXCL8 (also known as IL-8), which enhances the stem-like properties and migratory capacity of TSCs [8, 9]. In turn, TSCs promote TAM polarization toward the $CXCL8^+$ M2 phenotype through reciprocal signaling, thereby establishing a bidirectional positive feedback loop [10]. This CXCL8-dependent TAM-TSC immune stemness circuit has been documented in multiple solid tumors and is closely associated with increased tumor invasiveness and immune evasion [8, 11]. However, the existence, mechanistic basis, and functional significance of this loop in THCA have not yet been systematically investigated. Disrupting this reciprocal signaling network may therefore represent a promising therapeutic strategy to impede malignant progression and reverse the immunosuppressive TME [12, 13]. Currently, effective approaches capable of simultaneously targeting M2 TAMs and TSCs while modulating their interactive signaling pathways are lacking, highlighting an urgent need for innovative strategies that enable precise intervention in this immune stemness loop with substantial scientific and translational potential.

FAT1, an atypical cadherin, has recently been recognized as a tumor suppressor involved in the regulation of cell polarity, migration, and key oncogenic signaling pathways, including Wnt and Hippo [14, 15]. Multiple studies have reported that FAT1 is frequently downregulated in solid tumors, including hepatocellular carcinoma and colorectal cancer, and its loss is often associated with enhanced tumor stemness, increased metastatic potential, and poor prognosis [16, 17]. Existing evidence further suggests that FAT1 may participate in remodeling the immune microenvironment, particularly by regulating chemokine expression and macrophage polarization [18, 19]. Despite its therapeutic potential, the large and complex structure of the FAT1 protein presents substantial challenges for direct protein supplementation. In contrast, mRNA-based delivery strategies offer a promising alternative for restoring FAT1 expression. Owing to their rapid and transient protein expression, controllable immune activation, and minimal risk of genomic integration, mRNA therapeutics have gained increasing attention in the field of precision medicine. However, the clinical translation of mRNA-based therapies remains constrained by critical technical challenges, including delivery efficiency, targeting specificity, and *in vivo* stability [20, 21].

At present, direct evidence linking FAT1 to CXCL8/M2 TAMs remains limited. However, FAT1 plays an important role in the formation of an immunosuppressive TME. In glioblastoma, high FAT1 expression reduces the infiltration of T cells and monocytes while increasing the abundance of immunosuppressive cells [22]. FAT1 can also remodel the inflammatory cytokine profile secreted by tumor cells and stromal cells through signaling networks such as transforming growth factor beta (TGF-β) [23]. In addition, FAT1 has been reported to upregulate the expression of pro-inflammatory mediators, including COX2, IL-1β, and IL-6 [24]. These mechanisms promote tumor-associated signaling pathways and may thereby indirectly influence macrophage polarization as well as the expression and secretion of CXCL8 [25]. Based on this rationale, the present study aimed to investigate the functional role of FAT1 within the THCA TME, with a particular focus on its potential mechanism in regulating the immune stemness feedback loop between $CXCL8^+$ M2 TAMs and TSCs. We designed and constructed a cRGD-modified mesenchymal stem cell (MSC)-derived extracellular vesicle (EV)-liposome (LNP) hybrid nanosystem for FAT1 mRNA delivery (ELH@FAT1), to disrupt the pro-tumor interaction between TAMs and TSCs, remodeling the immune microenvironment, and suppressing tumor stemness and distant metastasis. This work not only expands mechanistic understanding of FAT1 function but also provides theoretical support and a novel technological approach for combined immunotherapy of THCA and other solid tumors. Furthermore, our findings hold translational potential for advancing mRNA-based nanomedicine in precision oncology and may offer a new therapeutic avenue for refractory THCA.

2 Experimental

2.1 Bioinformatics analysis of The Cancer Genome Atlas (TCGA)-THCA dataset

Transcriptomic data and corresponding clinical information for THCA were obtained from the Xiantao Academic platform, which integrates standardized data from TCGA and provides visualization and statistical analysis tools. The TCGA-THCA dataset, comprising 510 THCA samples and 58 normal thyroid tissues (n = 568), was downloaded for analysis. Data preprocessing, including normalization and batch-effect correction, was performed using the platform's built-in pipelines to ensure data consistency and comparability.

Clinical correlation analyses were conducted to evaluate the association between FAT1 expression and clinicopathological features, including survival status, residual tumor burden, extrathyroidal extension, histological subtype, and pathological stage. Pearson or Spearman correlation tests were applied as appropriate based on data distribution. Statistical analyses were performed using the stats and car packages in R, and data visualization was generated with "ggplot2" package. Variables that did not meet statistical assumptions were excluded from further analysis.

2.2 Single-cell RNA sequencing (scRNA-seq) and data analysis of THCA tumor samples in mouse models

To assess the impact of ELH@FAT1 treatment on tumor cellular composition and intercellular communication within the TME, thyroid tumor tissues from one mouse in the PBS-treated control group and one mouse in the ELH@FAT1-treated group were subjected to scRNA-seq. Excised tumor tissues were washed with ice-cold PBS, mechanically minced, and enzymatically digested at 37 °C using 1 mg/mL collagenase (Sigma-Aldrich, USA) for 10 min, followed by a 5 min digestion with trypsin/EDTA (Gibco, USA) to generate single-cell suspensions.

Single cells were captured and lysed using the Fluidigm C1 single-cell automated platform (Fluidigm, USA), followed by on-chip reverse transcription and cDNA amplification. Sequencing libraries were constructed and sequenced on the Illumina HiSeq 4000

platform using paired-end reads (2 × 75 bp), with an average depth of approximately 20,000 reads per cell. Raw sequencing data were processed using the Seurat package (v4.0.0). Cells with low quality were excluded based on the following criteria: 200 < nFeature_RNA < 5000 and mitochondrial gene content < 25%. Highly variable genes were identified, and the top 2000 genes were selected for downstream analyses.

2.3 Cell subpopulation clustering and marker gene analysis

Cell subpopulation identification and annotation were performed using the Seurat package (v4.0). Following normalization of the gene expression matrix, principal component analysis (PCA) was conducted, and the top 30 principal components were used for downstream analysis. Cell clustering was visualized using uniform manifold approximation and projection (UMAP). Based on established marker genes, including IL1B, CD163, and MRC1 for macrophages and CXCR4 and CD44 for TSCs, distinct cell subpopulations were annotated. The DimPlot function was applied to visualize the distribution of TSCs in the PBS and ELH@FAT1 treatment groups.

2.4 TAM typing and functional state analysis

To characterize the functional states of M2-type TAMs and TSCs following ELH@FAT1 treatment, single-cell transcriptomic data were analyzed for the expression of key marker genes (IL1B, MRC1, CD163, CXCR4, and CD44), as well as CXCL8 and its receptors CXCR1 and CXCR2. Comparative expression patterns between the PBS and ELH@FAT1 groups were visualized using Violin Plot and FeaturePlot functions.

2.5 Cell–cell interaction analysis

Cell–cell communication among TAMs, THCA cells, and TSCs was analyzed using the CellChat package (v1.5.0). Ligand–receptor interaction networks were inferred to compare intercellular signaling between the PBS and ELH@FAT1 groups. Pathway enrichment analysis was performed on the identified key signaling axes (CXCL8-CXCR1/2 and CCL2-CCR2) to elucidate the potential mechanisms of intercellular communication.

2.6 Isolation and identification of EVs

Human bone marrow-derived mesenchymal stem cells (BMSCs; AC340039, ATCC) were cultured for 48 h in Dulbecco's Modified Eagle Medium (DMEM; Sigma-Aldrich, USA) supplemented with 10% EV-depleted fetal bovine serum (FBS). Culture supernatants were collected and sequentially centrifuged at 500*g* for 10 min to remove cells and at 2000*g* for 10 min to eliminate cell debris. The clarified supernatant was then ultracentrifuged at 100,000*g* for 1 h at 4 °C. The resulting pellet was resuspended in PBS and subjected to a second ultracentrifugation under identical conditions for further purification. The final EV suspension was concentrated by centrifugation at 12,000*g* for 30 min at 4 °C, filtered through a 0.22 μm membrane, and either used immediately or stored at −80 °C. EV morphology was examined by transmission electron microscopy (TEM). EV samples were loaded onto carbon-coated copper grids, negatively stained with phosphotungstic acid (pH 6.8), and imaged using a Hitachi H-7650 TEM system (Hitachi, Japan). Particle size distribution and concentration were measured by nanoparticle tracking analysis (NTA; NanoSight LM10, Malvern Instruments, UK). The isolated EVs exhibited a mean diameter of approximately 112 nm with a narrow size distribution and a concentration of about 1×10^{11} particles/mL (Figs. S1(a) and S1(b) in the Electronic Supplementary Material (ESM)).

Western blot (WB) analysis was performed to detect EV-specific protein markers using antibodies against CD9 (ab223052, 1:500, Abcam, UK), CD63 (ab216130, 1:2000, Abcam, UK), TSG101 (ab30871, 1:1000, Abcam, UK), and Calnexin (ab22595, 1:100, Abcam, UK). The results indicated that CD9, CD63, and TSG101 were positively detected in EVs, whereas the endoplasmic reticulum marker Calnexin was absent, suggesting high purity of the isolated EVs (Fig. S1(c) in the ESM).

2.7 Construction of the ELH@FAT1

An ethanol-assisted membrane fusion strategy was employed to construct the MSC-derived EV-liposome hybrid nanosystem for FAT1 mRNA delivery. Liposomes were first prepared using the thin-film hydration-extrusion method. Briefly, phosphatidylcholine (PC; Sigma-Aldrich, USA), cholesterol, and DSPE-SS-PEG2000-cRGD (Ruixi Biology) were mixed at a molar ratio of 4:3:1 in chloroform to form a lipid film. After vacuum evaporation, the film was hydrated with PBS containing FAT1 mRNA or scrambled control mRNA, incubated at 65 °C for 10 min, and extruded 11 times through a 200 nm polycarbonate membrane to generate liposomes, designated as LNP@FAT1 and LNP@NC, respectively. MSC-derived EVs were isolated by ultracentrifugation combined with density gradient separation and quantified based on total protein content. EVs were mixed with liposomes at a protein mass ratio of 1:1, followed by the addition of 10% absolute ethanol. The mixture was incubated at 37 °C for 30 min to enhance membrane fluidity and promote vesicle fusion. Residual ethanol was removed using Amicon ultrafiltration tubes (Millipore, USA), yielding the final ELH@FAT1 nanosystem and the control ELH@NC. WB analysis confirmed that ELH@FAT1 retained canonical EV membrane protein markers (CD9, CD63, and TSG101), whereas these markers were absent in liposomes alone, indicating successful incorporation of EV membranes into the hybrid nanosystem (Fig. S1(d) in the ESM). To generate a non-cRGD-modified hybrid nanosystem, DSPE-SS-PEG2000 was substituted for DSPE-SS-PEG2000-cRGD using the same protocol, yielding iELH@FAT1.

2.8 TEM characterization

Nanoparticles (NPs) were diluted to 0.1 mg/mL, and 10 μL of the sample was applied onto carbon-coated copper grids. After incubation for 1 min, the grids were negatively stained with 7% uranyl acetate (pH 7.0, Sigma-Aldrich, USA) for 30 s, dried, and observed using a TEM (JEM-2100Plus, JEOL, Japan) operated at 200 kV.

2.9 Dynamic light scattering (DLS) and zeta potential measurement

NPs were diluted to 0.2 mg/mL, and the hydrodynamic diameter and zeta potential were measured at 25 °C using a Zetasizer Nano ZS particle analyzer (Malvern, UK). Each sample was measured in triplicate, and the mean particle size and surface charge were recorded.

2.10 Fluorescence resonance energy transfer (FRET) assay for fusion efficiency

Fusion efficiency between liposomes and EVs was evaluated using a FRET assay. Liposomes were labeled with NBD-PE (1 mol%,

Thermo Fisher Scientific, USA) and Rhodamine-PE (1 mol%, Avanti Polar Lipids, USA), mixed with EVs at varying mass ratios (LNP:EV = 0.125:1 to 2:1), and fused by sonication. Samples were excited at 488 nm, and emission spectra were recorded using a multifunctional microplate reader (Synergy H1, BioTek, USA) and a fluorescence spectrophotometer (F-7000, Hitachi, Japan). All samples were adjusted to 0.1 mg/mL and measured under identical conditions (excitation at 488 nm; emission range 500–650 nm; step size 2 nm). Enhanced FRET signals at 590 nm were observed in both ELH and ELH@FAT1 groups, indicating successful membrane fusion.

2.11 WB verification of fusion components

Total proteins from EVs, ELH, and ELH@FAT1 were extracted using RIPA lysis buffer, and 30 μg of protein per lane was subjected to sodium dodecyl sulfate-polyacrylamide gel electrophoresis (SDS-PAGE). After separation on 10% SDS-PAGE gels, proteins were transferred to nitrocellulose (NC) membranes. After blocking with 5% nonfat milk in TBST, membranes were incubated overnight at 4 °C with primary antibodies against EV markers (TSG101, CD63, and CD9), with Calnexin serving as a negative control. Membranes were then incubated with HRP-conjugated secondary antibodies (Abcam, UK), and protein bands were visualized using enhanced chemiluminescence (ECL). Images were captured using the ChemiDoc MP imaging system (Bio-Rad, USA).

2.12 mRNA protection and stability analysis

To evaluate the protective effect of ELH@FAT1 on FAT1 mRNA, free FAT1 mRNA or ELH@FAT1-encapsulated mRNA was incubated with either 10% FBS or RNase A (10 ng/mL) at 37 °C. Samples were collected at 1 and 5 min and at 3, 6, 12, and 24 h. Following release, mRNA integrity was analyzed by 1% agarose gel electrophoresis in Tris-acetate-EDTA (TAE) buffer at 120 V for 30 min. Gels were stained with GoldView nucleic acid dye and imaged using a gel documentation system (Tanon 2500, China).

2.13 mRNA release profile analysis

The release behavior of FAT1 mRNA from liposomes (LNP@FAT1) and ELH@FAT1 was evaluated using a dialysis method. Briefly, samples were loaded into dialysis bags (MWCO 100 kDa) and incubated in PBS (pH 7.4) containing 10% FBS at 37 °C with shaking at 100 rpm. At predetermined time points, the external buffer was collected, and the released mRNA was quantified by quantitative real-time polymerase chain reaction (qRT-PCR). The cumulative release profile was subsequently plotted.

2.14 Determination of mRNA loading capacity (LC) and encapsulation efficiency (EE)

The LC and EE of FAT1 mRNA in ELH@FAT1 NPs were quantified by RT-qPCR. Briefly, ELH@FAT1 was resuspended in RNase-free PBS at 1 mg/mL, and a 500 μL aliquot was centrifuged at 12,000*g* for 10 min at 4 °C to separate free mRNA. The supernatant containing unencapsulated mRNA and FAT1 mRNA standards (0.1–100 ng/μL, generated by *in vitro* transcription) was reverse transcribed using the PrimeScript™ RT Reagent Kit (Takara). qPCR was then performed on an ABI 7500 Real-Time PCR System with SYBR® Premix Ex Taq™ II (Takara) under the following conditions: 95 °C for 30 s, followed by 40 cycles of 95 °C for 5 s and 60 °C for 30 s. The concentration of free mRNA and total mRNA was calculated based on the Ct value-concentration standard curve. EE (%) and LC (μg mRNA/mg NP) were calculated according to the following equation (Eq. (1))

$$\text{Encapsulation efficiency (EE\%)} = \frac{\text{Total mRNA} - \text{Free mRNA}}{\text{Total mRNA}} \times 100\% \quad (1)$$

2.15 Stability assay in simulated physiological fluid

ELH, ELH@FAT1, and LNP samples were diluted to 0.2 mg/mL and incubated in PBS (pH 7.4) containing 10% FBS at 37 °C on a shaker at 100 rpm for 7 days. Samples were collected once daily, and particle size and zeta potential were measured using a Zetasizer Nano ZS90 to assess NP stability under simulated physiological conditions.

2.16 Cell culture and treatment

The THCA cell lines 8505C and HTH83 (Procell, CL-0496 and CL-0081), as well as the normal thyroid epithelial cell line Nthy-ori 3-1 (Procell, CL-0048), were used in this study. All cells were maintained in RPMI-1640 medium supplemented with 10% FBS (C0235, Beyotime) and 1% Penicillin-Streptomycin (PB180120, Procell) at 37 °C in a humidified incubator with 5% CO_2.

THP-1 human monocytes (ATCC, TIB-202) were differentiated into M0 macrophages by treatment with phorbol 12-myristate 13-acetate (PMA, 100 ng/mL) for 48 h, followed by polarization into M2-type TAMs using IL-4 (20 ng/mL) and IL-13 (20 ng/mL) for 24 h. The resulting TAMs were cocultured with 8505C cells to establish a TAM-TSC interaction model.

8505C cells were routinely cultured in RPMI-1640 medium (Gibco, USA) supplemented with 10% FBS (C0235, Beyotime) and 1% PB180120 (Procell) under 37 °C, 5% CO_2 conditions. To enrich the TSC subpopulation, a tumorsphere suspension culture method was applied. Briefly, 8505C cells were digested with trypsin and resuspended in DMEM/F12 medium (PM150315, Procell) supplemented with 20 ng/mL epidermal growth factor (EGF; E3477, Thermo Fisher), 20 ng/mL basic fibroblast growth factor (bFGF; 13256-029, Thermo Fisher), and 2% B27 serum-free supplement (A3582801, Thermo Fisher). Cells were seeded in ultra-low attachment plates (Corning, USA), with medium replaced every 3 days, and cultured for 7 days to generate primary spheres. The spheres were then mechanically dissociated and subjected to two additional rounds of suspension culture to obtain stably passaged spheres, which were defined as the TSC population [26].

2.17 Sphere formation assay

Cells were seeded at a density of 1×10^3 cells per well in ultra-low attachment 96-well plates (200 μL/well) and cultured for 7 days. Each experiment included three biological replicates and was independently repeated three times. Spheroid formation was assessed by inverted microscopy, and spheroids with diameters ≥ 50 μm were quantified. Both spheroid number and diameter were measured using ImageJ to evaluate cellular stemness.

2.18 Cell coculture and confocal uptake imaging

THCA cells (8505C and HTH83) and normal thyroid epithelial cells (Nthy-ori 3-1) were seeded on glass coverslips and incubated with ELH@FAT1 or non-targeted iELH@FAT1 containing Cy5-

labeled mRNA for 24 h at 37 °C. Cells were then washed, fixed with 4% paraformaldehyde (PFA) for 10 min, and rinsed with PBS. Cellular uptake was visualized using laser scanning confocal microscopy (Zeiss LSM 700), and fluorescence intensity was quantified using ZEN 2009 software. Cy5 fluorescence signals were calculated from at least three randomly selected fields.

2.19 Lysosome/endosome colocalization analysis (confocal microscopy)

8505C cells (1.2×10^5) were seeded in 6-well plates containing glass coverslips. After attachment, cells were incubated with Cy5-labeled ELH@FAT1 nanoparticles (30 μg/mL) for 15, 30, 60, or 120 min. Lysosomes and endosomes were labeled using LysoTracker Red DND-99 (75 nM, Thermo Fisher Scientific, L7528, USA) or Rab7-GFP (200 nM, Thermo Fisher Scientific, C10588) for 30 min, respectively. Cells were then fixed with 4% PFA (Sigma-Aldrich, USA) for 10 min, washed with PBS, and permeabilized with 0.1% Triton X-100 (Solarbio, China) at room temperature for 10 min. To block nonspecific binding, cells were incubated with 5% bovine serum albumin (BSA; Beyotime, China) for 30 min. Nuclei were counterstained with 4',6-diamidino-2-phenylindole (DAPI) (Beyotime, C1002, China) for 10 min. Images were acquired using a Zeiss LSM 980 confocal microscope (Carl Zeiss, Germany) at 400× magnification under fixed acquisition parameters.

2.20 Pearson's correlation coefficient (PCC) colocalization analysis

Quantitative colocalization analysis between ELH@FAT1 nanoparticles and endosomes or lysosomes was performed by calculating PCC using the Coloc 2 plugin in ImageJ (NIH, USA). Dual-channel correlation analysis was performed between the Cy5 signal (red channel) and LysoTracker or MitoTracker (green channel). For each group, five non-overlapping fields were randomly selected from three technical replicates. Images were background-subtracted and normalized before PCC values were calculated. The PCC ranges from −1 to 1, with higher values indicating stronger colocalization.

2.21 CCK-8 cell viability assay

Nthy-ori 3-1 cells were seeded in 96-well plates at a density of 5×10^3 cells per well and treated with 0, 10, 50, 100, or 200 μg/mL ELH@FAT1 for 48 h. After treatment, 10 μL of CCK-8 reagent (Dojindo, Japan) was added to each well and incubated for 2 h at 37 °C. Absorbance was measured at 450 nm using a BioTek Synergy H1 microplate reader, and cell viability was expressed as the percentage relative to the PBS control group. Each experiment was performed in triplicate.

2.22 Annexin V-FITC/propidium iodide (PI) flow cytometry apoptosis assay

Cells treated under the same conditions as the CCK-8 assay were harvested, washed with PBS, and stained using an Annexin V-FITC/PI apoptosis detection kit (BD Pharmingen, USA). Apoptotic cells were analyzed using a BD FACSAria Fusion flow cytometer, and data were processed with FlowJo v10 software.

2.23 WB detection of protein expression

Cells or tissue samples were harvested, and protein extraction methods were selected according to the target protein. Total protein was extracted using RIPA lysis buffer (R0278, Sigma-Aldrich, USA) supplemented with a protease inhibitor cocktail (P8340, Sigma-Aldrich, USA) and a phosphatase inhibitor cocktail (P0044, Sigma-Aldrich, USA), followed by lysis on ice for 30 min. Nuclear protein was extracted using a nuclear and cytoplasmic protein extraction kit (P0028, Beyotime, China) to separate cytoplasmic and nuclear fractions. Protein concentration was determined using a BCA assay (71285-M, Merck). Total protein was separated by SDS-PAGE and transferred onto polyvinylidene difluoride (PVDF) membranes (IEVH00005, Millipore). The PVDF membranes were blocked with BSA for 30 min and incubated with primary antibodies (Table S1 in the ESM), followed by HRP-conjugated goat anti-mouse IgG H&L (ab205719, Abcam, 1:5000) or HRP-conjugated goat anti-rabbit IgG (ab205718, Abcam, 1:5000) as secondary antibodies. Protein bands were visualized using an ECL detection reagent (P0018S, Beyotime) and imaged with the Bio-Rad ChemiDoc XRS+ system. The net gray values of the bands were quantified using ImageJ software.

2.24 Construction of a Transwell non-contact co-culture system

A Transwell non-contact co-culture system (0.4 μm pore size; Corning, USA) was established to investigate paracrine interactions between TAMs and TSCs. For TAM-mediated regulation of TSCs, 8505C cells (5×10^4 cells/well) were seeded in the lower chamber, while M2 macrophages differentiated from THP-1 cells (2×10^5 cells/well) were seeded in the upper chamber. Five experimental groups were included: THCA alone, THCA + M2, THCA + M2 + ELH@FAT1 (100 μg/mL), THCA + M2 + ELH@FAT1 + recombinant human CXCL8 (10 ng/mL), and THCA + M2 + anti-CXCL8 neutralizing antibody (2 μg/mL). ELH@FAT1, CXCL8, or anti-CXCL8 was added to the upper chamber to selectively act on M2 macrophages. After 24 h of co-culture, cells were collected for subsequent analyses.

To assess feedback regulation of macrophages by tumor stem-like cells, 8505C-derived TSCs were assigned to four groups: PBS, ELH@FAT1 (100 μg/mL), ELH@FAT1 + sh-NC, and ELH@FAT1 + sh-FAT1. TSCs and THP-1-derived M0 macrophages were seeded into the upper and lower chambers, respectively. ELH@FAT1 and lentiviral vectors were applied to TSCs, and after 24 h of co-culture, samples were harvested for downstream assays.

2.25 RT-qPCR analysis of gene expression

Total RNA was extracted using TRIzol reagent (T9424, Merck). For qPCR, cDNA was synthesized in PCR tubes with TransScript® II One-Step gDNA Removal and cDNA Synthesis SuperMix (AH311-02, TransGen). The amplification program consisted of an initial denaturation at 95 °C for 10 s, followed by 40 cycles of 95 °C for 10 s, 60 °C for 20 s, and 72 °C for 36 s. Relative expression levels were quantified using the $2^{-\Delta\Delta Ct}$ method. Primer sequences are listed in Table S2 in the ESM.

2.26 Enzyme-linked immunosorbent assay (ELISA)

CXCL8 levels in serum or cell supernatants were quantified using the CXCL8 ELISA Kit (ab7747, Abcam) following the manufacturer's protocol.

2.27 Immunofluorescence staining and confocal imaging

Immunofluorescence staining was performed to examine the expression and localization of CXCL8 and related markers in M2

TAMs at both cellular and tissue levels. For cell staining, treated cells were seeded onto glass coverslips, allowed to adhere overnight, fixed with 4% paraformaldehyde for 15 min, permeabilized with 0.1% Triton X-100 for 10 min, and blocked with 1% BSA for 30 min. For tissue staining, paraffin-embedded tumor sections were deparaffinized with xylene, rehydrated through graded ethanol, subjected to antigen retrieval in sodium citrate buffer (pH 6.0) at 95 °C for 30 min, and blocked with 1% BSA for 30 min. Subsequently, the samples were incubated overnight at 4 °C with the following primary antibody combinations: FAT1 (1:200, sc-53283, Santa Cruz) + VIM (1:200, ab92547, Abcam); FAT1 (1:200, sc-53283, Santa Cruz) + PanCK (1:200, ab270305, Abcam); FAT1 (1:200, sc-53283, Santa Cruz) + CD68 (1:200, ab125212, Abcam); or with rabbit anti-CD206 antibody (ab64693, 1:200, Abcam, UK) and mouse anti-CXCL8 antibody (ab18672, 1:100, Abcam, UK). The following day, samples were incubated with Alexa Fluor® 488-conjugated goat anti-rabbit IgG (ab150077, 1:1000, Abcam) and Alexa Fluor® 647-conjugated goat anti-mouse IgG (ab150115, 1:1000, Abcam) for 1 h at room temperature in the dark, followed by nuclear counterstaining with DAPI (ab104139, 1 μg/mL, Abcam) for 10 min. After PBS washing, the slides were mounted. Images were captured using a confocal microscope (LSM 700 or LSM 980, Zeiss, Germany) at 400× magnification, and processed with ZEN 2009 software (Carl Zeiss, Oberkochen, Germany).

2.28 Flow cytometric analysis of immune cell composition and TAM polarization phenotypes

To systematically evaluate immune cell subsets and TAM polarization within the TME, tumor tissues were collected, minced under sterile conditions, and digested in HBSS buffer (24020117, Thermo Fisher Scientific, USA) containing type IV collagenase (0.5 mg/mL) and DNase I (0.25 mg/mL) at 37 °C with shaking for 30 min. The resulting cell suspension was filtered through a 40 μm cell strainer and centrifuged at 400*g* for 10 min. Cell pellets were washed with PBS and incubated with TruStain FcX™ Fc receptor blocking solution for 10 min to reduce nonspecific antibody binding. Cells were then stained with antibodies against CD68 (ab201340, Abcam), CD163 (ab239338, Abcam), CD206 (ab270647, Abcam), CD86 (ab77226, Abcam), CD8 (301041, BioLegend), CD4 (300514, BioLegend), CD56 (318306, BioLegend), and FOXP3 (320114, BioLegend), followed by incubation in the dark for 30 min. Data acquisition was performed using a BD FACSAria Fusion flow cytometer (BD Biosciences, USA), and analysis was conducted with FlowJo software (v10.6, FlowJo LLC).

2.29 Transwell assay for cell migration

Transwell chambers (8.0 μm pore size, Corning, CLS3422, USA) were used to assess cell invasion ability. The inserts were precoated with Matrigel (354234, Corning, USA), diluted in serum-free medium, and incubated at 37 °C for 1 h to form a uniform gel layer. Cells were washed with PBS, resuspended in serum-free medium, and adjusted to a density of 1×10^5 cells/100 μL before being seeded into the upper chamber. The lower chamber was filled with 600 μL complete medium containing 10% FBS as a chemoattractant.

Following incubation at 37 °C with 5% CO_2 for 24–48 h, non-migrated cells on the upper surface of the membrane were removed with cotton swabs. Migrated cells were fixed with 4% paraformaldehyde for 30 min and stained with 0.1% crystal violet for 15 min. After washing, invaded cells were counted in five randomly selected fields under an inverted microscope. Results were expressed as the average number of migrated cells per field.

2.30 Animal models and housing conditions

Female BALB/c mice (6–8 weeks, #211, Beijing Vital River Laboratory Animal Technology Co., Ltd.), BALB/c-nu nude mice (#401, Beijing Vital River Laboratory Animal Technology Co., Ltd.), and NSG mice (NOD.Cg-Prkdc^{scid} Il2rg^{tm1Wjl}/SzJ [NSG], 6–8 weeks, female, NM-NSG-001, Shanghai Model Organisms Center, China) were used in this study. Animals were obtained from certified commercial suppliers and maintained in a specific pathogen-free (SPF) facility under controlled environmental conditions (22 ± 2 °C, 55% ± 10% relative humidity, and a 12 h light/dark cycle), with *ad libitum* access to standard chow and sterile water. All animal procedures were approved by the Institutional Animal Care and Use Committee of our institution (approval No. 2024-HSYY-308).

2.31 Construction of humanized immune system (HIS)-reconstituted mice

Four-week-old female NSG mice were subjected to a single 1.5 Gy γ-irradiation to deplete endogenous hematopoietic cells. Within 24 h after irradiation, 1.0×10^5–2.0×10^5 human umbilical cord blood-derived CD34$^+$ hematopoietic stem/progenitor cells (hCD34$^+$ HSCs; #50-197-5778, Fisher Scientific, USA) were injected via the tail vein to establish HIS mice. Human umbilical cord blood (hUCB) was first processed by Ficoll-Paque Plus density gradient centrifugation (#17-1440-02, Cytiva, USA) to isolate mononuclear cells (MNCs), followed by purification of CD34$^+$ cells using a human CD34 MicroBead Isolation Kit (#130-046-702, Miltenyi Biotec, Spain). After purification, the CD34$^+$ fraction was analyzed by flow cytometry, and only cell preparations with ≥ 90% purity were used for transplantation. At weeks 8, 10, and 12 post-transplantation, peripheral blood mononuclear cells (PBMCs) were collected, and the proportion of human CD45$^+$ cells was determined by flow cytometry. HIS reconstitution was considered successful when the percentage of hCD45$^+$ cells was ≥ 25% [27, 28].

2.32 Establishment and treatment of THCA mouse models

Humanized NSG mice were acclimatized for one week prior to tumor implantation. Enriched 8505C cells were resuspended in Matrigel at a 1:1 (v/v) ratio, and 100 μL of the suspension containing 5×10^6 cells was subcutaneously injected into the right dorsal flank using a 27G needle. When tumor volume reached approximately 100 mm^3, the mice were randomly assigned into seven groups (n = 6 per group): PBS, ELH@FAT1, ELH@FAT1 + sh-NC, ELH@FAT1 + sh-FAT1, ELH@FAT1 + rhCXCL8, LNP, and ELH@NC. Treatments were administered via tail vein injection, with each mouse receiving 50 μg/kg of PBS or ELH@FAT1, in combination with 1×10^6 TU/mouse sh-FAT1 or 1 μg/mouse rhCXCL8. Tumor size was measured weekly using a vernier caliper, and the short diameter (a) and long diameter (b) were recorded. Tumor volume was calculated using the formula: $\pi \times (a^2b)/6$. On day 28 after the final treatment, mice were sacrificed, tumors were excised, and tumor weight was determined using an analytical balance (ME204T, Mettler Toledo, Switzerland). The final tumor mass was recorded for statistical analysis.

For the lung metastasis model, 1×10^6 8505C cells suspended in 100 μL PBS were injected intravenously into humanized NSG mice via the tail vein. Mice were subsequently randomized into five

treatment groups: PBS, ELH@FAT1, ELH@FAT1 + sh-NC, ELH@FAT1 + sh-FAT1, and ELH@FAT1 + rhCXCL8. After 28 days of treatment, mice were sacrificed, and lungs were harvested, fixed, paraffin-embedded, and subjected to hematoxylin and eosin (H&E) staining. Metastatic nodules were examined under a light microscope and quantified per mouse [28–30].

2.33 *In vivo* biosafety evaluation

To assess the *in vivo* biosafety of the ELH@FAT1 nanosystem, mice were randomly divided into groups (n = 6 per group) and intravenously injected with 200 μL PBS, empty ELH NPs, or ELH@FAT1 NPs (1 mg/kg, single dose). On day 7, the mice were sacrificed, and blood as well as major organs (liver, spleen, kidney, lung, and heart) were collected for subsequent biochemical, hematological, and histological analyses.

2.34 Serum biochemical analysis

Blood samples were collected by cardiac puncture and centrifuged at 3000 rpm for 10 min at 4 °C to obtain serum. Serum levels of alanine aminotransferase (ALT), aspartate aminotransferase (AST), blood urea nitrogen (BUN), and creatinine (CRE) were measured using commercial assay kits (MAK052, MAK467, MAS008, and MAK080; all from Sigma-Aldrich, USA).

2.35 Hematological analysis

Whole blood samples were collected into EDTA-coated anticoagulant tubes and analyzed within 2 h using an automated veterinary hematology analyzer (BC-2800Vet, Mindray, China). Red blood cell (RBC) count, white blood cell (WBC) count, hemoglobin (HGB) concentration, and neutrophil (NEU) count were measured. All analyses were completed within 2 h to minimize hemolysis and cell aggregation.

2.36 Establishment of THCA xenograft model and NP tracing

BALB/c-nu nude mice were subcutaneously injected in the right dorsal flank with 5×10^6 8505C THCA cells suspended in 100 μL PBS (n = 6 per group). When tumor volumes reached approximately 100 mm^3, mice were intravenously injected with DiR-labeled ELH@FAT1 or iELH@FAT1 NPs (DiR: 1 μg/200 μL, Sigma-Aldrich, USA). *In vivo* fluorescence imaging was performed at 0.5, 3, 12, and 24 h post-injection. At 24 h, mice were euthanized, and tumors together with major organs (heart, liver, spleen, lung, and kidney) were harvested for *ex vivo* fluorescence imaging. Fluorescence intensity was quantitatively analyzed using Living Image software [27].

2.37 Immunohistochemistry (IHC) and quantitative analysis

Tumor and lung tissues were fixed in 10% neutral buffered formalin for 48 h, paraffin-embedded, and sectioned at a thickness of 4 μm. Sections were deparaffinized, rehydrated, and subjected to antigen retrieval in citrate buffer (pH 6.0) at 95 °C for 30 min. Endogenous peroxidase activity was quenched with 3% H_2O_2, followed by blocking with 5% BSA for 30 min.

The sections were incubated overnight at 4 °C with the following primary antibodies: FAT1 (ab228965, 1:100, Abcam, UK), Ki-67 (ab15580, 1:200, Abcam, UK), CD163 (ab182422, 1:200, Abcam), CD206 (ab64693, 1:200, Abcam), Thyroglobulin (ab168344, 1:200, Abcam), PAX8 (ab191870, 1:500, Abcam), SOX2 (ab97959, 1:200, Abcam), Granzyme B (ab4059, 1:200, Abcam), IFN-γ (ab231036, 1:200, Abcam), VIM (ab92547, 1:200, Abcam), PanCK (ab270305, 1:200, Abcam), and CD68 (ab125212, 1:200, Abcam). On the following day, the sections were incubated with HRP-conjugated secondary antibody (ab205718, 1:500, Abcam) for 1 h, followed by color development with DAB (ZSGB-BIO, China) and counterstaining with hematoxylin. Slides were dehydrated and mounted, and images were captured using a Zeiss Axioscope microscope at 200× or 400× magnification, with a scale bar of 50–100 μm. For each sample, at least three randomly selected fields were analyzed. The numbers of positively stained and total cells were quantified using ImageJ software, and IHC results were expressed as the percentage of positive cells (positive cells/total cells × 100%).

2.38 Statistical software and data analysis

Bioinformatics analyses were performed using R software (v4.2.1) with RStudio (v2022.12.0-353), and data preprocessing was conducted using Perl (v5.30.0). Statistical analyses were performed using GraphPad Prism (v10.0). Sample sizes for *in vivo* experiments were determined using Prism's built-in power analysis tool based on preliminary tumor inhibition data (α = 0.05, β = 0.2), ensuring 80% statistical power. Sample sizes for *in vitro* experiments were calculated using the same criteria. Data were expressed as mean ± standard deviation. Comparisons between two groups were performed using independent-sample t-tests. For multiple group comparisons and single-cell sequencing data analyses, one-way ANOVA followed by Bonferroni post hoc correction was applied. For repeated measurements at different time points, two-way ANOVA with Bonferroni correction was employed. Statistical significance was set at $P < 0.05$.

3 Results

3.1 Public database analysis reveals FAT1 loss promotes stemness and metastasis in THCA

Publicly available TCGA-THCA datasets were analyzed to evaluate FAT1 expression patterns and their clinical relevance. FAT1 mRNA expression was significantly reduced in THCA tissues compared with normal thyroid tissues (Fig. S2(a) in the ESM). Moreover, FAT1 expression progressively declined from pathological stage I to stage IV (Fig. S2(b) in the ESM), suggesting a potential tumor-suppressive role of FAT1 during THCA progression. Consistently, FAT1 expression also decreased across residual tumor categories (R0–R2) (Fig. S2(c) in the ESM), indicating a possible association between FAT1 loss, tumor recurrence, and therapeutic resistance.

In patients with different pathological stages, FAT1 expression was significantly correlated with both N and M classifications. FAT1 expression was highest in normal tissues but progressively decreased from N0 to N1 (Fig. S2(d) in the ESM), implying that FAT1 may influence lymph node metastasis. Moreover, FAT1 expression was markedly lower in M1 compared with M0 patients (Fig. S2(e) in the ESM), suggesting that reduced FAT1 expression may promote distant metastasis.

Further analysis of FAT1 expression across different histological subtypes of THCA (Classical, Follicular, Tall Cell) showed that FAT1 expression was lowest in the Tall Cell subtype (Fig. S2(f) in the ESM). Given that the Tall Cell variant is characterized by higher

aggressiveness and poorer clinical outcomes, this finding suggests that FAT1 downregulation may contribute to the malignant phenotype of this subtype. Immune infiltration analysis using the CIBERSORT algorithm further showed that tumors with high FAT1 expression exhibited significantly increased infiltration of $CD8^+$ T cells and natural killer (NK) cells, whereas regulatory T cells (Tregs) and monocytes were relatively reduced compared with the low-FAT1 group (Fig. S2(h) in the ESM). These results indicate that FAT1 expression is associated with a more immunoactive TME.

In summary, FAT1 was markedly downregulated in THCA tissues, and its reduced expression may facilitate tumor cell invasion and metastasis.

3.2 Successful construction of the ELH@FAT1 nanosystem

Based on our previous finding that MSCs-EVs carrying GTF2I upregulate FAT1 expression in THCA and suppress tumor stemness [31], we aimed to design an ELH@FAT1 nanosystem (Fig. 1(a)). The nanosystem was generated by ultrasound-assisted fusion, in which MSCs-EVs served as the structural framework and LNPs encapsulated FAT1 mRNA. To further enhance targeting, the particles were modified with DSPE-SS-PEG2000-cRGD.

TEM revealed that ELH@FAT1 exhibited a uniform spherical morphology with well-defined boundaries and a continuous lipid bilayer, consistent with successful EV-LNP fusion. Compared with EVs or LNPs alone, ELH@FAT1 displayed a slightly increased particle size and more homogeneous surface characteristics (Fig. 1(b)). DLS analysis showed that empty ELH particles had an average diameter of ~ 145 nm, whereas ELH@FAT1 averaged ~ 150 nm. By contrast, EVs and LNPs measured ~ 112 and ~ 123 nm, respectively, indicating that FAT1 mRNA loading slightly increased particle size (Figs. 1(c) and 1(d)). Zeta potential analysis demonstrated values of −12.4 mV for EVs and +18.6 mV for LNPs, while both empty ELH and ELH@FAT1 exhibited Zeta potentials of approximately −10 mV. This profile, being closer to EVs, is favorable for achieving stable, long-circulating distribution *in vivo* (Fig. 1(e)).

Fusion efficiency and component integration were further validated by FRET analysis (Fig. 1(f)). Compared with LNPs alone, both ELH and ELH@FAT1 exhibited significantly enhanced FRET signals, indicating efficient membrane fusion between EVs and LNPs. Notably, the highest FRET intensity was observed at an EV-to-LNP ratio of 1:1, suggesting optimal fusion efficiency under this condition (Fig. 1(g)). Further fluorescence spectroscopy analysis revealed that both ELH and ELH@FAT1 displayed a distinct FRET signal peak at 590 nm, accompanied by a reduction in fluorescence intensity at 540 nm, which is consistent with the successful formation of an EV-LNP nanosystem (Fig. 1(h)). Based on these findings, the optimal EV-to-LNP ratio of 1:1 was selected for preparing ELH@FAT1.

To verify whether ELH@FAT1 formed stable NPs capable of effectively protecting FAT1 mRNA from nuclease degradation, a stability assay was conducted. The stability of free mRNA and ELH@FAT1-encapsulated mRNA against serum and RNase was assessed at different time points (1 min, 5 min, 3 h, 6 h, 12 h, and 24 h) (Fig. 1(i)). Electrophoresis analysis revealed no detectable leakage of mRNA, indicating that FAT1 mRNA was efficiently encapsulated within the NPs. When free mRNA and ELH@FAT1 were incubated with 10% FBS or RNase, the free mRNA underwent rapid degradation, whereas ELH@FAT1 maintained a stable structure without mRNA leakage even after 24 h, demonstrating that encapsulation within NPs effectively prevented ribonuclease-mediated degradation. Furthermore, RNase degradation assays showed that free FAT1 mRNA was almost completely degraded within 1 h, leaving less than 20% intact mRNA, whereas more than 70% of FAT1 mRNA remained intact after 12 h when protected by ELH@FAT1 (Fig. 1(i)). These results indicate that the nanosystem effectively delayed mRNA degradation and enhanced delivery stability.

In addition, to evaluate the stability of ELH@FAT1 under physiological conditions, the NPs were incubated in simulated body fluid (pH 7.4, PBS + 10% FBS) for 7 days, with particle size and zeta potential monitored. The results showed that the particle size remained at 150 ± 5 nm and the zeta potential stabilized around −10 mV, confirming that ELH@FAT1 maintained excellent stability under physiological conditions (Figs. 1(j) and 1(k)). The average drug LC of FAT1 mRNA in ELH@FAT1 NPs was 25 ± 3 μg mRNA/mg NP, with an EE of 90% ± 4%, indicating a high level of mRNA LC and EE (Fig. 1(l)).

Collectively, these results demonstrate that ELH@FAT1 is a well-defined, stable EV-liposome hybrid nanosystem with high fusion efficiency, robust mRNA protection, and favorable physicochemical properties, providing a reliable platform for efficient FAT1 mRNA delivery.

3.3 ELH@FAT1 nanosystem enables efficient targeted delivery of FAT1 mRNA

To evaluate the targeting capacity, lysosomal escape, and biosafety of the ELH@FAT1 nanosystem, its distribution, delivery efficiency, and potential cytotoxicity in different cell types were systematically examined (Fig. 2(a)). Confocal microscopy revealed robust intracellular Cy5 fluorescence in THCA cell lines (8505C and HTH83) following treatment with ELH@FAT1, whereas significantly weaker signals were observed with non-cRGD-modified iELH@FAT1. In contrast, minimal uptake was detected in normal thyroid epithelial cells (Nthy-ori 3-1), indicating that cRGD modification conferred enhanced tumor-selective targeting (Fig. 2(b)).

Subcellular localization analysis further demonstrated efficient endosomal escape of ELH@FAT1. Time-course confocal imaging showed that ELH@FAT1 entered early endosomes within 15–30 min and progressively escaped from lysosomes between 60 and 120 min after internalization in 8505C cells (Figs. 2(c) and 2(d)). PCC analysis confirmed a time-dependent decrease in colocalization between ELH@FAT1 and lysosomes after 30 min, indicating effective lysosomal escape (Figs. 2(e) and 2(f)). This property is critical for cytoplasmic release of FAT1 mRNA and subsequent protein translation.

To determine whether the ELH@FAT1 nanosystem possessed delivery capability at the cellular level, 8505C and HTH83 cells were treated with different concentrations of ELH@FAT1 (10, 50, 100, and 200 μg/mL), followed by assessment of FAT1 expression. RT-qPCR analysis revealed that FAT1 mRNA levels increased significantly in a concentration-dependent manner (Fig. 2(g)). Consistently, WB analysis showed that FAT1 protein expression also rose in a dose-dependent fashion (Figs. 2(h) and 2(i)), indicating that ELH@FAT1 effectively delivered FAT1 and promoted its expression in tumor cells.

To evaluate the biosafety of ELH@FAT1, its cytotoxic effects on

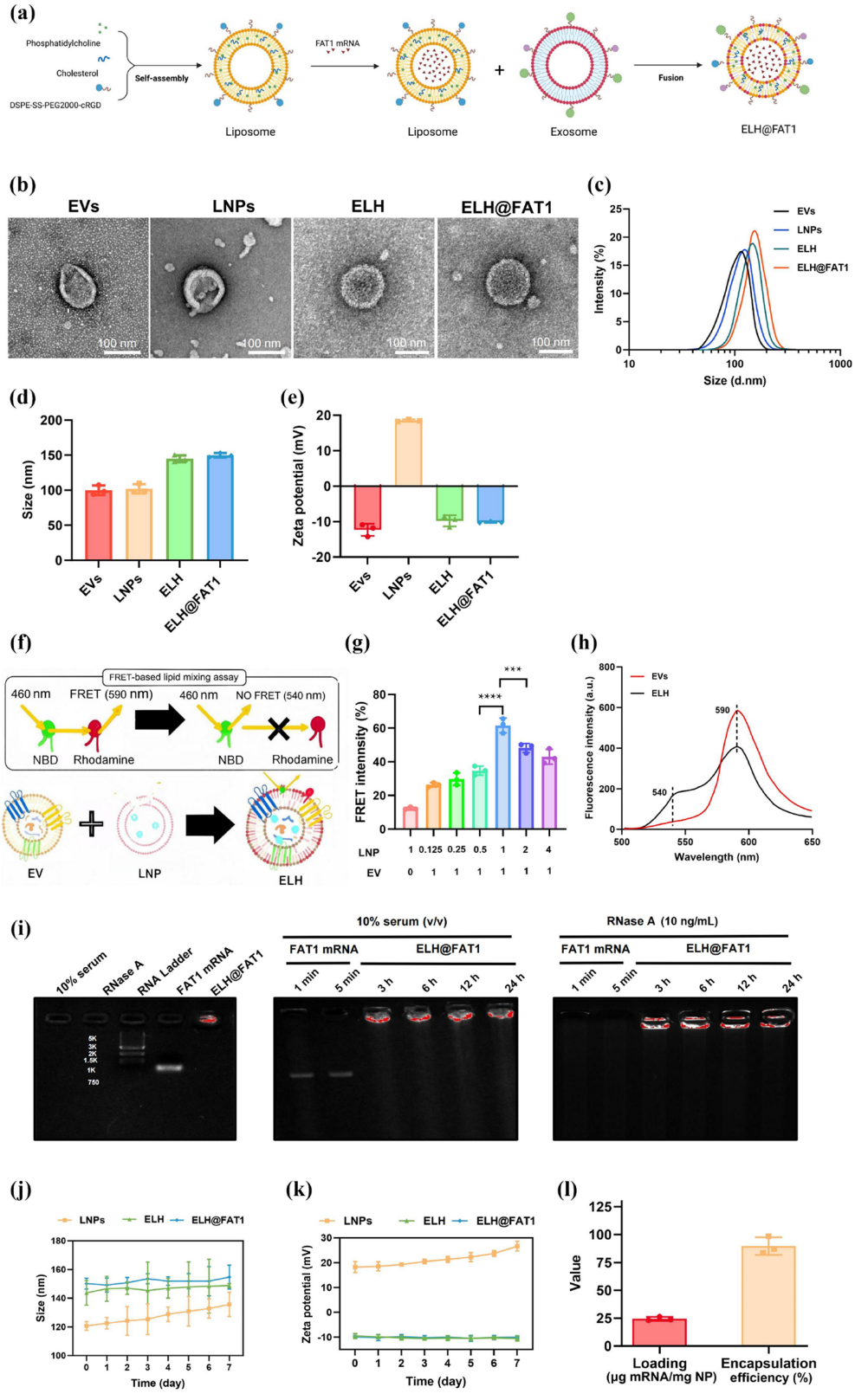

Figure 1 Construction and physicochemical characterization of the ELH@FAT1 nanosystem. (a) Schematic illustration of NP preparation. (b) Morphological characteristics of NPs observed by TEM, scale bars = 100 nm. (c, d) Particle size of EVs, LNPs, empty ELH, and ELH@FAT1 measured by DLS. (e) Zeta potential of EVs, LNPs, empty ELH, and ELH@FAT1 determined by DLS. (f) Schematic diagram of the principle for evaluating EV-LNP fusion efficiency using FRET. (g) Comparison of fusion efficiency at different EV:LNP ratios based on FRET signal intensity. (h) Fluorescence spectrum analysis of FRET signal changes in ELH and EVs. (i) Stability of free FAT1 mRNA and ELH@FAT1 in serum and RNase. (j) Stability assessment of NP size and (k) Zeta potential after 7 days of incubation under simulated physiological conditions (PBS with 10% FBS, pH 7.4). (l) FAT1 mRNA LC and EE in ELH@FAT1 NPs determined by RT-qPCR. Experiments were repeated three times. $^{***}P < 0.001$, $^{****}P < 0.0001$.

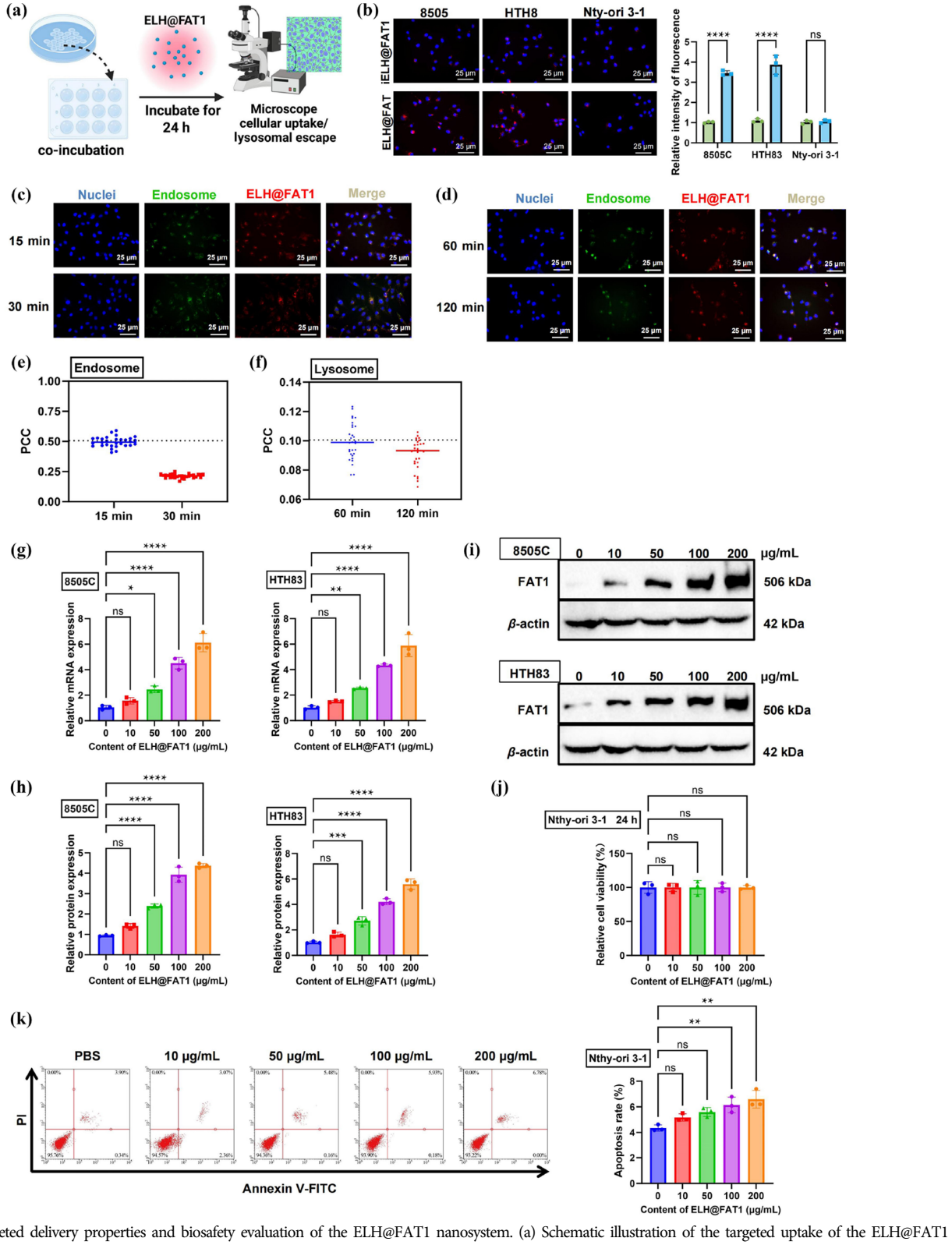

Figure 2 Targeted delivery properties and biosafety evaluation of the ELH@FAT1 nanosystem. (a) Schematic illustration of the targeted uptake of the ELH@FAT1 nanosystem. (b) Confocal microscopy images showing the uptake capacity of iELH@FAT1 and ELH@FAT1 in THCA cells (8505C, HTH83) and normal thyroid cells (Nthy-ori 3-1), with quantification of Cy5 fluorescence intensity, scale bars = 25 μm. (c) Representative confocal laser scanning microscopy images of ELH@FAT1 incubated with 8505C cells for 15 and 30 min, scale bars = 25 μm. (d) Representative confocal laser scanning microscopy images of ELH@FAT1 incubated with 8505C cells for 60 and 120 min, scale bars = 25 μm. PCC analysis of ELH@FAT1 colocalization with (e) endosomes (corresponding to panel (c)) and (f) lysosomes (corresponding to panel (d)). (g) FAT1 mRNA expression levels in 8505C and HTH83 cells treated with different concentrations of ELH@FAT1, detected by RT-qPCR. (h) FAT1 protein expression in 8505C and HTH83 cells treated with different concentrations of ELH@FAT1, measured by (i) WB. (j) Viability of normal cells treated with varying concentrations of ELH@FAT1, determined by CCK-8 assay. (k) Apoptosis rates of normal cells under different treatment conditions, assessed by Annexin V-FITC/PI flow cytometry. Cell experiments were repeated three times. ns, not significant, $^{*}P < 0.05$, $^{**}P < 0.01$, $^{***}P < 0.001$, $^{****}P < 0.0001$.

normal thyroid cells (Nthy-ori 3-1) were examined. CCK-8 assays showed that cell viability remained above 90% even at the highest tested concentration (200 μg/mL), with no detectable cytotoxicity (Fig. 2(j)). Similarly, Annexin V-FITC/PI double-staining flow cytometry revealed no significant increase in apoptosis at any tested concentration (Fig. 2(k)), further confirming the favorable *in vitro* safety profile of ELH@FAT1.

Collectively, these results demonstrate that ELH@FAT1 achieves efficient and selective tumor cell uptake, effective lysosomal escape, robust restoration of FAT1 expression, and minimal cytotoxicity, thereby providing a solid foundation for subsequent *in vivo* therapeutic evaluation.

3.4 ELH@FAT1 nanosystem exhibits favorable *in vivo* safety and achieves targeted delivery

To comprehensively evaluate the *in vivo* biosafety of the ELH@FAT1 nanosystem, mice were intravenously injected with PBS, ELH, or ELH@FAT1, followed by multidimensional safety assessment after seven days (Fig. S3(a) in the ESM). H&E staining revealed no evidence of tissue disorganization, inflammatory infiltration, necrosis, or fibrotic alterations in major organs, including the liver, spleen, kidney, heart, and lungs, across all groups (Fig. S3(b) in the ESM).

Serum biochemical analysis further confirmed the absence of systemic toxicity. Levels of ALT, AST, CRE, and URE showed no significant differences between the ELH and ELH@FAT1 groups compared with the PBS control (Fig. S3(c) in the ESM). Similarly, hematological examination demonstrated that RBC count, WBC count, HGB, and NEU levels remained comparable among the three groups (Fig. S3(d) in the ESM). To exclude potential inflammatory or immune activation, serum cytokine levels of IL-6, tumor necrosis factor-alpha (TNF-α), and interferon-gamma (IFN-γ) were measured by ELISA, revealing no significant elevation in the ELH@FAT1 group relative to PBS-treated controls (Fig. S3(e) in the ESM). Collectively, these findings demonstrate that ELH@FAT1 does not induce inflammatory responses or hematological toxicity *in vivo*.

To validate the tumor-targeting capability of ELH@FAT1, a subcutaneous THCA xenograft nude mouse model was established, and DiR-labeled iELH@FAT1 or ELH@FAT1 NPs were administered via tail vein injection to monitor their biodistribution in real time (Fig. S4(a) in the ESM). *In vivo* imaging system (IVIS) imaging revealed that, 24 h post-injection, ELH@FAT1 preferentially accumulated at the tumor site, where fluorescence intensity was markedly higher than that observed in the iELH@FAT1 group (Fig. S4(b) in the ESM). Quantitative fluorescence analysis further confirmed that tumor tissue signal intensity was significantly elevated in the ELH@FAT1 group compared with iELH@FAT1 (Fig. S4(c) in the ESM).

IHC staining revealed strong upregulation of FAT1 protein in tumor tissue of the ELH@FAT1 group, while expression in non-tumor tissues remained unchanged (Fig. S4(d) in the ESM). Consistently, RT-qPCR analysis of multiple tissues revealed a significant increase in FAT1 mRNA levels specifically in tumor tissue, with no detectable changes in the liver, kidney, lung, or heart (Fig. S4(e) in the ESM), indicating effective tumor-targeted delivery. Co-immunostaining of tumor sections for FAT1 together with pan-cytokeratin (PanCK), CD68, and vimentin (VIM) further confirmed that FAT1 expression was predominantly localized within tumor cells rather than stromal or immune compartments (Fig. S4(f) in the ESM).

Collectively, these results demonstrate that ELH@FAT1 exhibits excellent *in vivo* biocompatibility, achieves selective tumor accumulation, and enables efficient, tumor-specific expression of FAT1 within the THCA TME, underscoring its strong translational potential as a targeted mRNA delivery platform.

3.5 ELH@FAT1 nanosystem effectively suppresses THCA growth and distant metastasis *in vivo*

To evaluate the antitumor efficacy of the ELH@FAT1 nanosystem *in vivo*, a humanized subcutaneous THCA mouse model was established with seven groups: PBS control, ELH, ELH@FAT1, LNP, LNP@NC, LNP@FAT1, and ELH@NC, followed by intravenous administration (Fig. 3(a)). Longitudinal monitoring of tumor growth revealed that ELH treatment alone did not significantly inhibit tumor progression compared with PBS controls. In contrast, ELH@FAT1 treatment resulted in a marked reduction in tumor volume relative to the ELH group. Moreover, ELH@FAT1 exhibited significantly greater tumor growth inhibition than both LNP and ELH@NC controls (Fig. 3(b)). Consistently, measurements of terminal tumor weight demonstrated that tumors in the ELH@FAT1 group were significantly lighter than those in the ELH group, as well as the LNP and ELH@NC groups (Fig. 3(c)). H&E staining further showed that tumor tissues from the ELH@FAT1 group exhibited disorganized cellular architecture and markedly increased necrotic areas, indicating a pronounced therapeutic effect (Fig. 3(d)).

To assess the inhibitory effect of ELH@FAT1 on distant metastasis, a lung metastasis model was generated via tail vein injection, followed by histological evaluation (Fig. 3(e)). H&E staining revealed abundant metastatic nodules in the lungs of mice treated with PBS or ELH, whereas ELH@FAT1 treatment markedly reduced both the number and size of pulmonary metastatic lesions (Fig. 3(f)). Quantitative analysis confirmed that ELH@FAT1 treatment significantly decreased the mean number of nodules per mouse lung (Fig. 3(g)). Moreover, IHC staining of THCA markers in lung tissue, including TG and PAX8, revealed markedly lower expression levels in metastatic lesions from the ELH@FAT1 group compared with the ELH group (Fig. 3(h)).

To further evaluate whether ELH@FAT1 successfully upregulated FAT1 expression *in vivo*, IHC and RT-qPCR were performed to assess FAT1 levels in tumor tissues. Both FAT1 protein and mRNA expression were significantly elevated in tumors from the ELH@FAT1 group relative to the ELH group (Figs. 3(i) and 3(j)). Concurrently, the expression of stemness-associated markers SOX2, octamer-binding transcription factor 4 (OCT4) and Nanog homeobox (Nanog) was markedly reduced in the ELH@FAT1 group (Fig. 3(k)), suggesting that restored FAT1 expression may inhibit tumor stemness.

In addition, TUNEL staining was conducted to assess apoptosis in tumor tissues. The number of TUNEL-positive cells was significantly higher in the ELH@FAT1 group than in the ELH group (Fig. 3(l)), indicating that ELH@FAT1 induced programmed cell death. IHC analysis of Ki-67 further demonstrated that the proliferative index of tumor tissues was markedly decreased in the ELH@FAT1 group (Fig. 3(m)), supporting its inhibitory effect on tumor growth.

In summary, the ELH@FAT1 nanosystem effectively delivered

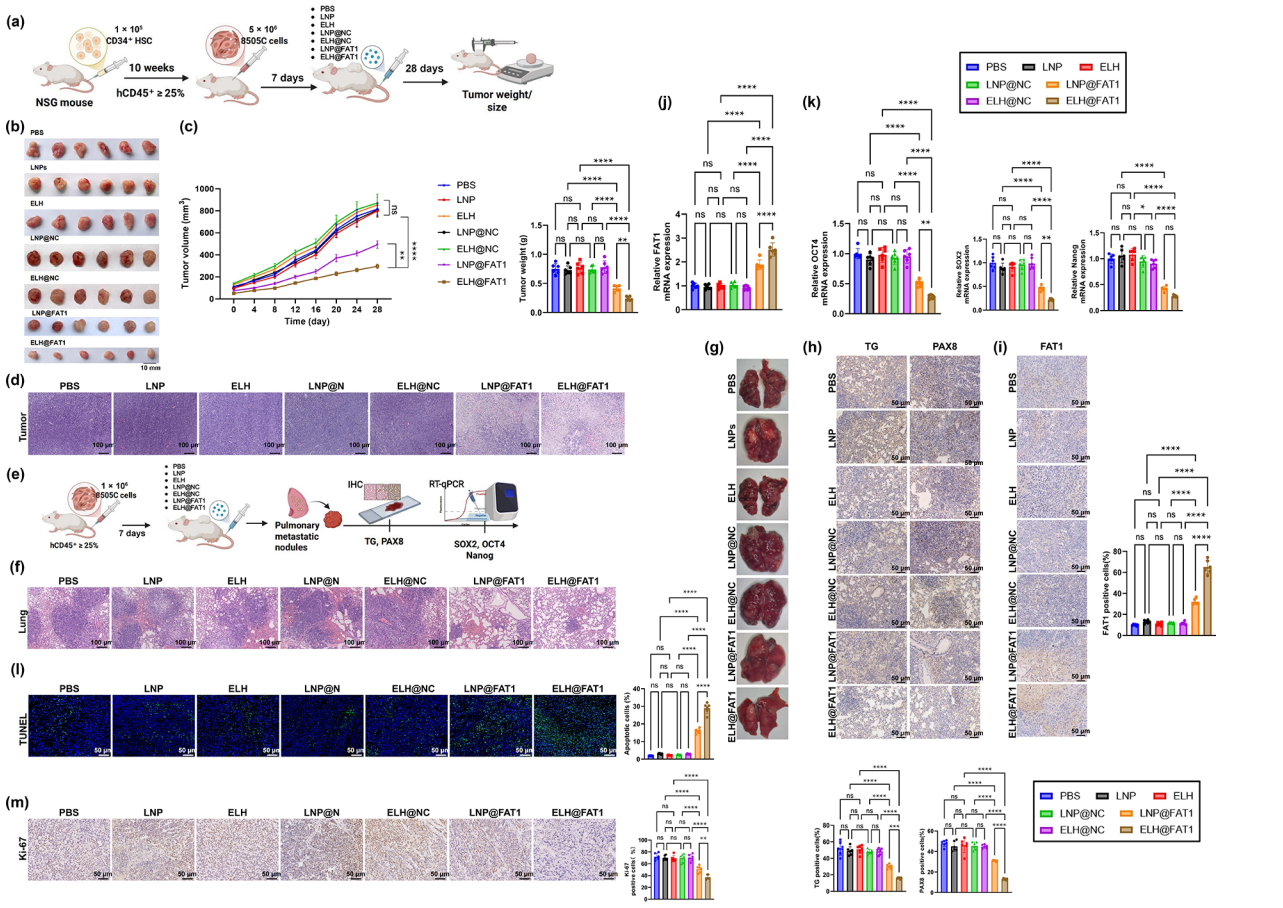

Figure 3 ELH@FAT1 nanosystem suppresses THCA growth and metastasis *in vivo*. (a) Schematic workflow of the study evaluating the effects of ELH@FAT1 on tumor progression in a subcutaneous THCA model. (b) Caliper measurements of tumor volume changes in each group. (c) Final tumor collection and weight comparison. (d) H&E staining of tumor tissues, scale bars = 100 μm. (e) Schematic workflow of the study evaluating the effects of ELH@FAT1 on tumor progression in a lung metastasis model. (f) H&E staining of metastatic lung nodules, scale bar = 100 μm. (g) Quantitative analysis of the number of lung metastatic nodules. (h) IHC staining of human THCA markers TG and PAX8 in lung tissues, scale bars = 50 μm. (i) IHC detection of FAT1 protein expression in tumor tissues, scale bars = 50 μm. (j) RT-qPCR analysis of FAT1 mRNA expression in tumor tissues. (k) RT-qPCR analysis of SOX2, OCT4, and Nanog mRNA expression in tumor tissues. (l) TUNEL staining of apoptotic cells in tumor tissues, scale bars = 50 μm. (m) IHC detection of Ki-67 expression in tumor tissues, scale bars = 50 μm. Each group included six mice. ns, not significant, $^{*}P < 0.05$, $^{**}P < 0.01$, $^{***}P < 0.001$, $^{****}P < 0.0001$.

FAT1 mRNA *in vivo*, restored FAT1 expression, and consequently suppressed THCA growth and lung metastasis.

3.6 Single-cell sequencing reveals that ELH@FAT1 reshapes the TME by disrupting TAM-TSC interaction networks

To systematically assess the impact of ELH@FAT1 on macrophage polarization and tumor-immune interactions within the TME, THCA xenograft tissues from the PBS and ELH@FAT1 treatment groups were dissociated into single-cell suspensions and subjected to scRNA-seq. After quality control, a total of 8197 high-quality cells were retained for downstream analysis, including 4042 cells from the PBS group and 4155 cells from the ELH@FAT1 group (Fig. 4(a)). Unsupervised clustering using Seurat combined with UMAP dimensionality reduction identified 11 major cell populations, including TSCs, M1 and M2 macrophages, fibroblasts, endothelial cells, and dendritic cells (Figs. 4(b) and 4(c), and Table S3 in the ESM). In the PBS group, the proportion of M2 macrophages was markedly higher than in the ELH@FAT1 group, suggesting that FAT1 upregulation may suppress tumor progression by reducing immunosuppressive cell subsets (Figs. 4(d) and 4(e)).

Differential expression analysis of macrophage subsets showed that M2 polarization-associated gene MRC1 was significantly downregulated following ELH@FAT1 treatment, whereas the pro-inflammatory M1 marker IL1B was markedly upregulated. Moreover, expression of CXCL8, which was enriched in M2 macrophages in the PBS group, was substantially decreased after ELH@FAT1 treatment (Figs. 4(f)–4(h)), indicating that CXCL8^{+} M2 macrophages constitute a key subpopulation targeted by ELH@FAT1.

Further annotation divided M2 macrophages into CXCL8^{+} M2 and CXCL8^{-} M2 subsets (Fig. S5(a) in the ESM). Ligand–receptor interaction and pathway enrichment analysis revealed that M2 macrophages in the PBS group were significantly enriched in the CXCL8 signaling axis and the immunosuppressive CCL2-CCR2 pathway (Figs. S5(b) and S5(c) in the ESM). In contrast, these pathways were strongly inhibited in the ELH@FAT1 group, accompanied by activation of M1-associated chemotactic and pro-inflammatory signaling, such as TNF-TNFRSF1A (Fig. S5(d) in the ESM). These findings indicate that ELH@FAT1 suppresses CXCL8^{+} M2 polarization, thereby reprogramming M2 macrophages toward an M1 phenotype and disrupting the immunosuppressive

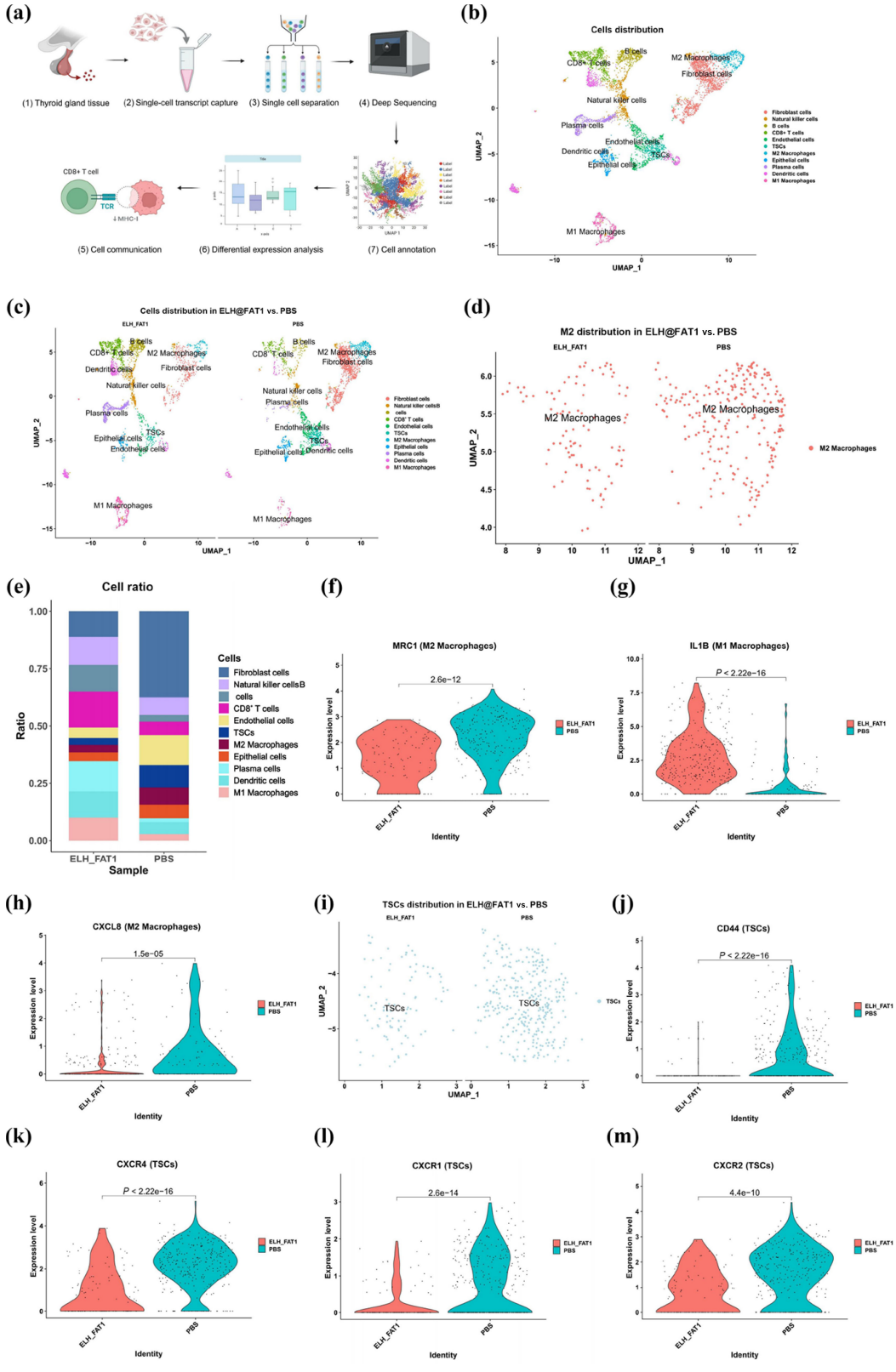

Figure 4 Single-cell analysis annotation of THCA. (a) Workflow of single-cell analysis in THCA. (b) Annotation of 11 cell types in THCA. (c) Annotation of 11 cell types in the PBS group and ELH@FAT1-treated group of THCA. (d) Distribution of M2 macrophages in the PBS and ELH@FAT1-treated groups. (e) Bar plot showing the distribution of 11 cell types in the PBS and ELH@FAT1-treated groups of THCA. (f) Significant upregulation of the M2 marker gene MRC1 in the PBS group. (g) Significant upregulation of the M1 marker gene IL1B in the ELH@FAT1-treated group. (h) Significant downregulation of CXCL8 in the ELH@FAT1-treated group. (i) Distribution of TSCs in the PBS and ELH@FAT1-treated groups. (j) Significant upregulation of the TSC marker gene CD44 in the PBS group. (k) Significant upregulation of the TSC marker gene CXCR4 in the PBS group. (l) Significant downregulation of the CXCL8 receptor CXCR1 in the ELH@FAT1-treated group. (m) Significant downregulation of the CXCL8 receptor CXCR2 in the ELH@FAT1-treated group.

microenvironment.

To further elucidate the functional consequences of CXCL8⁺ M2 macrophage modulation on tumor stemness, we examined the interaction networks between CXCL8⁺ M2 macrophages and TSCs. UMAP visualization revealed a significantly lower proportion of TSCs in the ELH@FAT1 group compared with the PBS group (Fig. 4(i)), suggesting that FAT1 upregulation may suppress the expansion of stem-like cells by interfering with CXCL8⁺ M2 macrophage-TSC interactions. Differential expression analysis showed that stemness-associated genes CD44 and CXCR4 were significantly downregulated in TSCs from the ELH@FAT1 group (Figs. 4(j) and 4(k)). Moreover, the CXCL8 receptors CXCR1 and CXCR2, which were highly expressed in TSCs from the PBS group, were significantly reduced in the ELH@FAT1 group (Figs. 4(l) and 4(m)), indicating diminished responsiveness of TSCs to CXCL8-mediated signaling.

Ligand–receptor interaction mapping further demonstrated that TAM-TSC communication in the PBS group was dominated by the CXCL8-CXCR1/2 axis, forming a positive feedback loop that sustained tumor stemness. This interaction network was effectively disrupted by ELH@FAT1 treatment, accompanied by enhanced IFN-mediated signaling between M1 macrophages and TSCs (Figs. S6(a) and S6(b) in the ESM), reflecting a shift from immunosuppressive to pro-inflammatory crosstalk.

In conclusion, ELH@FAT1 upregulated FAT1 expression, thereby blocking supportive signals from CXCL8⁺ M2 macrophages to TSCs, disrupting the interaction network that sustains tumor stemness, and profoundly remodeling the immune-stemness microenvironment to inhibit malignant progression.

3.7 *In vivo* evidence that ELH@FAT1 upregulates FAT1 to suppress CXCL8 expression and secretion in TAMs

In the THCA xenograft mouse model, we compared FAT1 expression and immune microenvironmental changes in tumor tissues from the PBS control group, the ELH group, the ELH@FAT1 group, the LNP group, and the ELH@NC group (Fig. 5(a)). IHC revealed that expression of the M2 macrophage markers CD206 and CD163 was markedly reduced in the ELH@FAT1 group, whereas no significant suppression of these markers was observed in the ELH group compared with ELH@FAT1. Moreover, relative to the LNP and ELH@NC groups, the proportion of M2-type TAMs was markedly reduced, whereas the proportion of CD86⁺ M1-type TAMs was significantly increased in the ELH@FAT1 group (Fig. 5(b)).

Multicolor flow cytometry further demonstrated that, relative to the PBS group, the proportion of M2-type TAMs was significantly

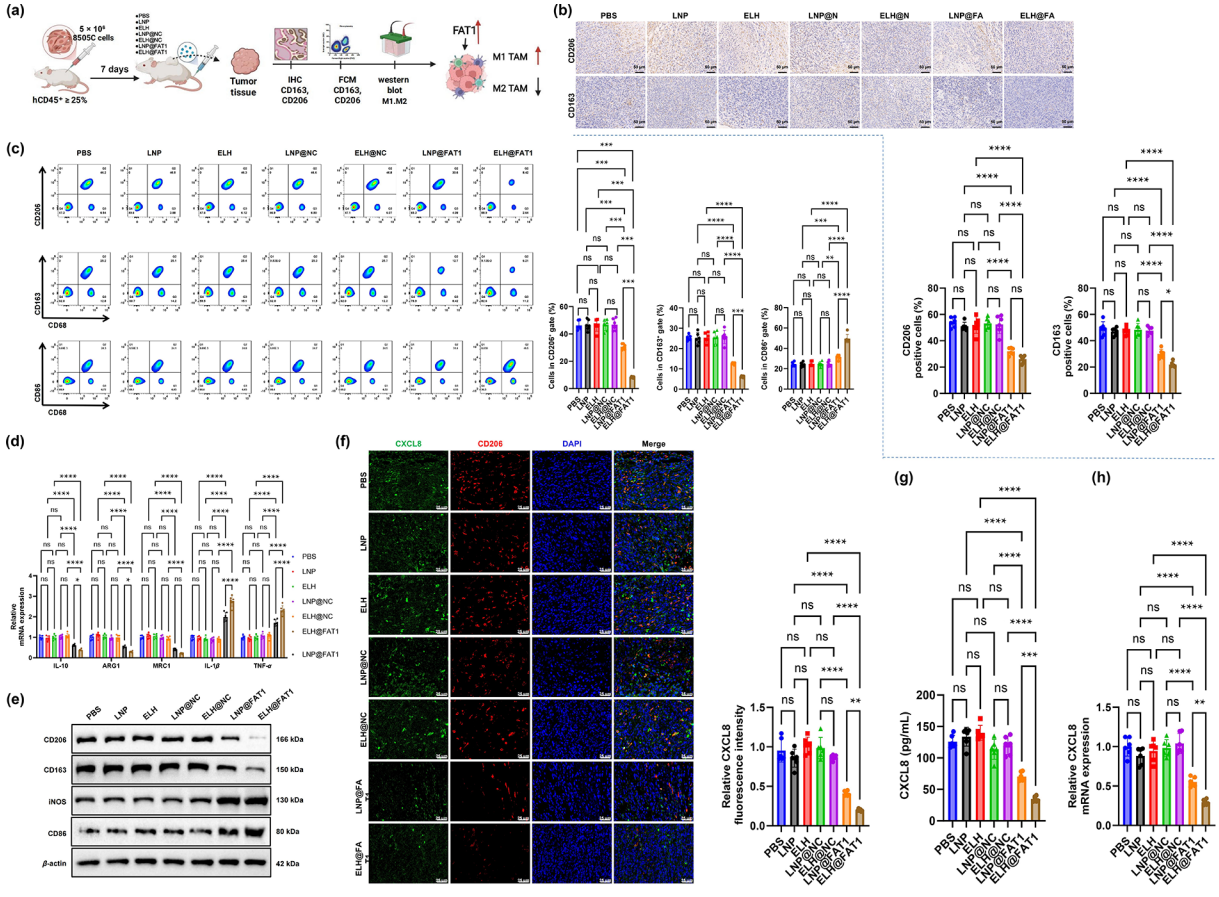

Figure 5 *In vivo* evidence that ELH@FAT1 upregulates FAT1 to suppress CXCL8 expression and secretion in M2-type TAMs. (a) Schematic of the experimental design evaluating the regulatory effect of ELH@FAT1 on the tumor immune microenvironment. (b) IHC showing the expression of M2-type TAM markers CD206 and CD163 in tumor tissues across groups (scale bars = 50 μm). (c) Multicolor flow cytometry analysis of CD86⁺ M1-type and CD206⁺ M2-type TAM proportions in tumor tissues. (d) RT-qPCR analysis of M1-associated factors (IL-1β, TNF-α) and M2-associated factors (IL-10, ARG1, MRC1) in tumor tissues. (e) WB analysis of CD206, CD163, CD86, and iNOS protein levels in tumor tissues across groups. (f) Immunofluorescence double staining (CD206 and CXCL8) showing CXCL8 expression in tumor tissues (scale bars = 25 μm). (g) ELISA quantification of CXCL8 secretion in tumor tissues. (h) RT-qPCR analysis of CXCL8 expression in tumor tissues. Each group contained six mice. ns indicates no significant difference between groups; ns, not significant, $^{*}P < 0.05$, $^{**}P < 0.01$, $^{***}P < 0.001$, $^{****}P < 0.0001$.

decreased and the proportion of $CD86^+$ M1-type TAMs was significantly increased in the ELH@FAT1 group. By contrast, the ELH group did not exhibit these changes compared with the ELH@FAT1 group. Moreover, relative to the LNP and ELH@NC groups, the ELH@FAT1 group displayed a pronounced decrease in M2-type TAMs and a concomitant increase in $CD86^+$ M1-type TAMs (Fig. 5(c)). Consistent with these findings, RT-qPCR analysis showed no significant alterations in M2-related factors in the ELH group relative to PBS, whereas in the ELH@FAT1 group, expression of IL-10, ARG1, and MRC1 was markedly downregulated, while proinflammatory factors IL-1β and TNF-α were significantly upregulated. Furthermore, compared with the LNP and ELH@NC groups, the ELH@FAT1 group exhibited significantly reduced expression of IL-10, ARG1, and MRC1, accompanied by significantly increased expression of IL-1β and TNF-α (Fig. 5(d)).

WB analysis further corroborated these results. Compared with the PBS group, the ELH@FAT1 group exhibited significant downregulation of CD206 and CD163, alongside a marked increase in CD86 and iNOS levels. In contrast, the ELH group showed no significant reduction in M2 polarization-associated proteins relative to ELH@FAT1. Moreover, relative to the LNP and ELH@NC groups, the ELH@FAT1 group showed significantly reduced expression of CD206 and CD163 and significantly elevated expression of CD86 and iNOS (Fig. 5(e)). Immunofluorescence double staining revealed that CXCL8 signals in $CD206^+$ TAMs were strongly diminished in the ELH@FAT1 group compared with PBS, suggesting that M2 TAMs primarily secreted CXCL8 and that ELH@FAT1 markedly suppressed this secretion. No obvious changes were detected in the ELH group. In addition, compared with the LNP and ELH@NC groups, CXCL8 signals in $CD206^+$ TAMs were markedly reduced in the ELH@FAT1 group, further supporting the notion that ELH@FAT1 effectively inhibits CXCL8 secretion from M2-type TAMs (Fig. 5(f)). ELISA further confirmed that CXCL8 protein levels in tumor tissue homogenates were significantly reduced in the ELH@FAT1 group (Fig. 5(g)). Similarly, RT-qPCR demonstrated that CXCL8 mRNA levels in tumor tissues from the ELH@FAT1 group were significantly lower than those in the PBS, LNP, ELH, and ELH@NC groups (Fig. 5(h)).

In summary, ELH@FAT1 upregulation of FAT1 effectively suppressed both the expression and secretion of CXCL8 in M2-type TAMs.

3.8 ELH@FAT1 suppresses CXCL8 to attenuate TAM-induced stemness and migration of THCA

To determine whether ELH@FAT1 regulates THCA cell phenotypes by suppressing CXCL8 secretion from M2-type TAMs, we established a non-contact Transwell co-culture system with the following groups: THCA alone, THCA+M2, THCA+M2+ELH@FAT1, THCA+M2+ELH@FAT1+rhCXCL8 recombinant protein, and THCA+M2+ELH@FAT1+anti-CXCL8 neutralizing antibody. EMT, stemness characteristics, and migratory capacity of THCA cells were subsequently evaluated (Fig. 6(a)).

WB analysis of EMT-related proteins revealed that, compared with THCA alone, the THCA+M2 group exhibited significant upregulation of the mesenchymal markers N-cadherin and Vimentin, alongside reduced expression of the epithelial marker E-cadherin. These alterations were markedly reversed by ELH@FAT1 treatment, restored by rhCXCL8 supplementation, and further reinforced by CXCL8 neutralization (Fig. 6(b)). RT-qPCR results were consistent with WB findings, confirming that ELH@FAT1 treatment suppressed EMT and stemness features in THCA cells (Fig. 6(c)).

Sphere formation assays and WB detection of stemness-associated proteins further supported these results. In the THCA+M2 group, tumor spheres were larger and more numerous, accompanied by marked upregulation of SOX2, OCT4, and NANOG. ELH@FAT1 treatment significantly reduced sphere formation capacity and stemness marker expression, while rhCXCL8 addition counteracted these effects (Figs. 6(d) and 6(e)). Flow cytometry revealed that the proportion of $CD133^+$ cells increased significantly in the THCA+M2 group, declined after ELH@FAT1 treatment, and rose again with rhCXCL8 supplementation (Fig. 6(f)).

Transwell migration assays showed that, compared with THCA alone, the THCA+M2 group exhibited significantly enhanced migration, which ELH@FAT1 markedly suppressed. This inhibitory effect was partially reversed by rhCXCL8 and further reinforced by the neutralizing antibody (Fig. 6(g)). ELISA analysis of culture supernatants demonstrated that ELH@FAT1 significantly reduced CXCL8 levels in the lower chamber, confirming effective inhibition of TAM-derived CXCL8 secretion (Fig. 6(h)).

In summary, ELH@FAT1 upregulated FAT1 to inhibit CXCL8 secretion from M2-type TAMs, thereby suppressing CXCL8-mediated EMT induction, tumor stemness maintenance, and migratory capacity. These findings establish the FAT1-CXCL8 axis as a critical regulator of TAM-THCA interactions.

3.9 ELH@FAT1 suppresses TSC-induced expression and secretion of CXCL8 in M2-like macrophages

To determine whether THCA TSCs promote macrophage polarization toward an M2 phenotype and induce CXCL8 expression and secretion, we established a non-contact Transwell co-culture system with the following groups: M0, TSC+M0, TSC+ELH@FAT1+M0, TSC+ELH@FAT1+sh-NC+M0, and TSC+ELH@FAT1+sh-FAT1+M0 (Fig. S7(a) in the ESM).

Immunofluorescence staining demonstrated that CD206 expression was markedly increased in the TSC+M0 group compared with M0 macrophages alone, indicating that TSCs effectively promoted macrophage polarization toward an M2-like phenotype. ELH@FAT1 treatment substantially reduced CD206 expression in macrophages co-cultured with TSCs, whereas FAT1 knockdown restored CD206 levels, suggesting that FAT1 upregulation counteracts TSC-driven M2 polarization (Fig. S7(b) in the ESM). RT-qPCR analysis further showed that TSCs significantly increased the transcription of M2-associated factors (CD206, CD163, ARG1, IL-10) in macrophages. Compared with the TSC group, these factors were markedly downregulated in the TSC+ELH@FAT1 group. sh-NC intervention did not alter this trend, whereas the TSC+ELH@FAT1+sh-FAT1 group again exhibited pronounced upregulation of these factors, confirming that FAT1 expression levels determined the ability of TSCs to drive macrophage M2 polarization (Fig. S7(c) in the ESM). Flow cytometric analysis further validated these findings, revealing a significant increase in the proportion of $CD68^+CD163^+$ M2-like macrophages in the TSC+M0 group, which was reduced by ELH@FAT1 treatment and reinstated following FAT1 knockdown (Fig. S7(d) in the ESM).

ELISA revealed that CXCL8 secretion by macrophages was substantially elevated in the TSC group. In contrast, the

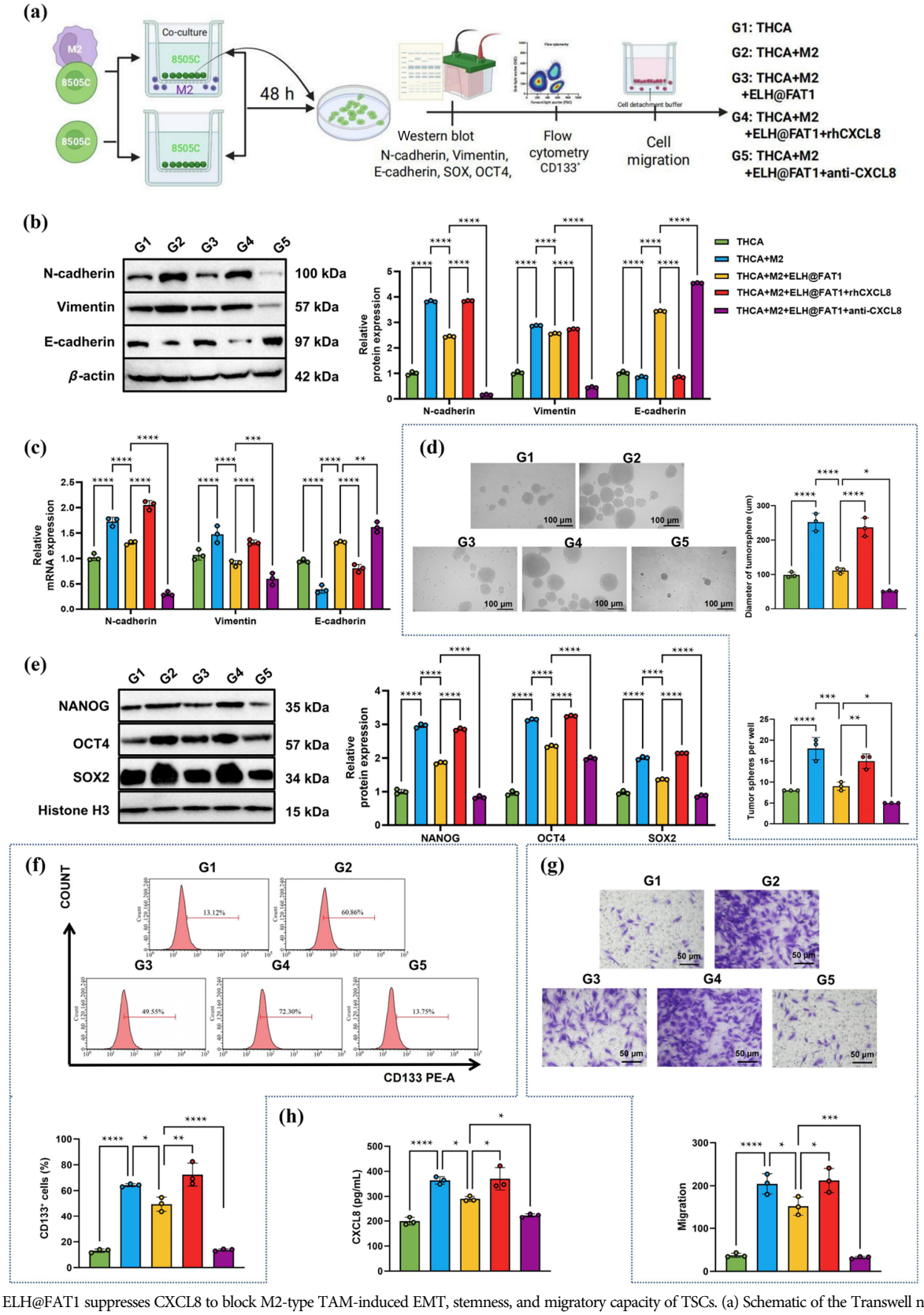

Figure 6 ELH@FAT1 suppresses CXCL8 to block M2-type TAM-induced EMT, stemness, and migratory capacity of TSCs. (a) Schematic of the Transwell non-contact co-culture system used to assess the effects of M2-type TAMs on TSC phenotypes, with six experimental groups. (b) WB analysis of E-cadherin, N-cadherin, and Vimentin protein expression. (c) RT-qPCR analysis of E-cadherin, N-cadherin, and Vimentin mRNA levels. (d) Sphere formation assay showing differences in spheroid size and number among groups (scale bars = 100 μm). (e) WB analysis of SOX2, OCT4, and NANOG protein expression. (f) Flow cytometry analysis of the proportion of $CD133^+$ TSCs. (g) Transwell assay assessing TSC migration across groups (scale bars = 50 μm). (h) ELISA quantification of CXCL8 protein secretion in the lower chamber medium. All cell experiments were performed in triplicate. $^*P < 0.05$, $^{**}P < 0.01$, $^{***}P < 0.001$, $^{****}P < 0.0001$.

TSC+ELH@FAT1 group showed markedly reduced CXCL8 expression, with no evident changes in the sh-NC group. Notably, sh-FAT1 intervention restored CXCL8 secretion to high levels, suggesting that FAT1 negatively regulated TSC-induced CXCL8 expression and thereby contributed to immune microenvironment modulation (Fig. S7(e) in the ESM). WB analysis further confirmed that FAT1 silencing restored the expression of M2 polarization-associated proteins, including CD206 and ARG1, in macrophages co-cultured with TSCs (Fig. S7(f) in the ESM).

Taken together, these results demonstrate that ELH@FAT1 suppresses TSC-driven M2 polarization and CXCL8 expression/secretion through FAT1 upregulation, thereby disrupting the TSC-TAM immune stemness positive feedback loop and weakening the formation of an immunosuppressive TME.

3.10 ELH@FAT1 inhibits the CXCL8 axis to disrupt immune stemness interactions and suppress metastasis

In a THCA xenograft mouse model, five groups—PBS, ELH@FAT1, ELH@FAT1+sh-NC, ELH@FAT1+sh-FAT1, and ELH@FAT1+rhCXCL8—were established to systematically evaluate whether FAT1 regulated immune stemness interactions through the CXCL8 axis (Fig. 7(a)).

IHC revealed that tumors from the ELH@FAT1 group exhibited robust upregulation of FAT1 expression, accompanied by marked reductions in the M2 TAM marker CD206 and the stemness-associated factors SRY-box transcription factor 2 (SOX2) and Nanog, indicating effective disruption of the immune-stemness positive feedback loop. In contrast, FAT1 silencing or CXCL8 supplementation restored CD206 and stemness marker expression, thereby re-establishing an immunosuppressive and stemness-enriched tumor state (Fig. 7(b)). Consistently, RT-qPCR analysis demonstrated significant downregulation of CXCL8, IL-10, ARG1, and SOX2 in the ELH@FAT1 group, whereas these genes were re-elevated following FAT1 knockdown or CXCL8 supplementation (Fig. 7(c)), reinforcing the role of FAT1 in disrupting immune-stemness crosstalk through CXCL8 suppression.

Multicolor flow cytometry of the tumor immune microenvironment revealed that the ELH@FAT1 group displayed significantly higher proportions of $CD8^+$ T cells and NK cells, along with reduced proportions of Tregs and M2 TAMs. However, FAT1 knockdown or CXCL8 supplementation diminished immune-activating populations and restored Tregs and M2 TAMs (Fig. 7(d)). Dual immunofluorescence further confirmed that CXCL8 originated predominantly from $CD206^+$ TAMs, with its signal markedly attenuated in the ELH@FAT1 group, while CXCL8 supplementation restored its expression in M2 TAMs (Fig. 7(e)).

A pulmonary metastasis model was further established with ELH@FAT1 and CXCL8 interventions (Fig. 8(a)). In this model, H&E staining revealed that the number of metastatic lesions in lung tissues was markedly reduced in the ELH@FAT1 group, accompanied by downregulation of the TSC marker PAX8 and the stemness factor SOX2. In contrast, the ELH@FAT1+sh-FAT1 and ELH@FAT1+rhCXCL8 groups exhibited a significant increase in lung metastatic nodules, with PAX8 and SOX2 expression restored (Fig. 8(b)). Quantitative analysis confirmed that ELH@FAT1 treatment significantly decreased the number of lung metastases, whereas FAT1 silencing or CXCL8 supplementation attenuated this anti-metastatic effect (Fig. 8(c)). Kaplan-Meier survival analysis showed that mice in the ELH@FAT1 group had a significantly prolonged survival time, while FAT1 knockdown or CXCL8 supplementation reversed this survival benefit (Fig. 8(d)).

To further investigate whether the CXCL8 axis contributes to FAT1-mediated immune evasion, the expression of T cell exhaustion markers was examined. Tumors from the ELH@FAT1 group exhibited significantly reduced expression of PD-1, LAG3, and TIM-3, indicating alleviation of T cell exhaustion and restoration of immune function. In contrast, FAT1 knockdown or CXCL8 supplementation reinstated the expression of these immune checkpoint molecules (Fig. 8(e)). Consistently, IHC demonstrated markedly enhanced signals of Granzyme B and IFN-γ in the ELH@FAT1 group, whereas their expression was diminished in the FAT1 knockdown and rhCXCL8 groups (Fig. 8(f)), further confirming that inhibition of CXCL8 restored T cell functionality and cytotoxic activity.

Collectively, these findings demonstrate that FAT1 suppresses $CXCL8^+$ M2 TAMs, thereby disrupting the positive feedback loop between TAMs and TSCs that sustains stemness and immune suppression, while simultaneously restoring T cell activity and limiting immune evasion.

4 Discussion

FAT1, an atypical cadherin, has been recognized as a tumor suppressor in multiple solid malignancies [14, 15]. Previous studies have primarily focused on hepatocellular carcinoma, gastric cancer, and colorectal cancer, demonstrating that FAT1 inhibits tumor cell proliferation and metastasis through pathways such as Hippo and Wnt [16, 18]. However, in THCA, the expression profile of FAT1, its functional role, and its relationship with the immune microenvironment remain poorly understood. By integrating TCGA-based bioinformatic analysis with experimental validation, the present study provides the first evidence that FAT1 is significantly downregulated in THCA tissues and that its loss is closely associated with an immunosuppressive tumor phenotype. These findings suggest that FAT1 not only functions as an intracellular signaling regulator but also exerts previously unappreciated immunomodulatory effects within the TME, thereby extending its role beyond tumor-intrinsic regulation to immune-tumor crosstalk.

The immune stemness feedback interaction between $CXCL8^+$ M2 TAMs and TSCs has been reported in other solid tumors [9, 32], but direct evidence in THCA has remained limited. Through both *in vitro* and *in vivo* models, this study validated the existence of this feedback loop and, for the first time, confirmed that the restoration of FAT1 expression could disrupt its activity. Rescue experiments further revealed that exogenous CXCL8 supplementation partially abrogated the antitumor effects induced by FAT1 upregulation, highlighting the FAT1-CXCL8 axis as a critical regulatory node governing tumor stemness maintenance and immune evasion. In contrast to earlier studies that primarily emphasized the chemotactic properties of CXCL8, our findings identify CXCL8 as a central signaling mediator within a bidirectional TAM-TSC activation loop, thereby substantially expanding its functional significance within the TME.

The negative regulatory effect of FAT1 on CXCL8 expression was functionally validated in this study, as FAT1 upregulation markedly suppressed CXCL8 secretion in M2-TAMs. Previous studies have suggested that elevated FAT1 expression in tumor cells may modulate pro-inflammatory signaling pathways such as NF-κB or STAT3 [19, 33]. Activation of NF-κB and STAT3 in tumor cells typically alters paracrine and cell–cell signaling, thereby influencing

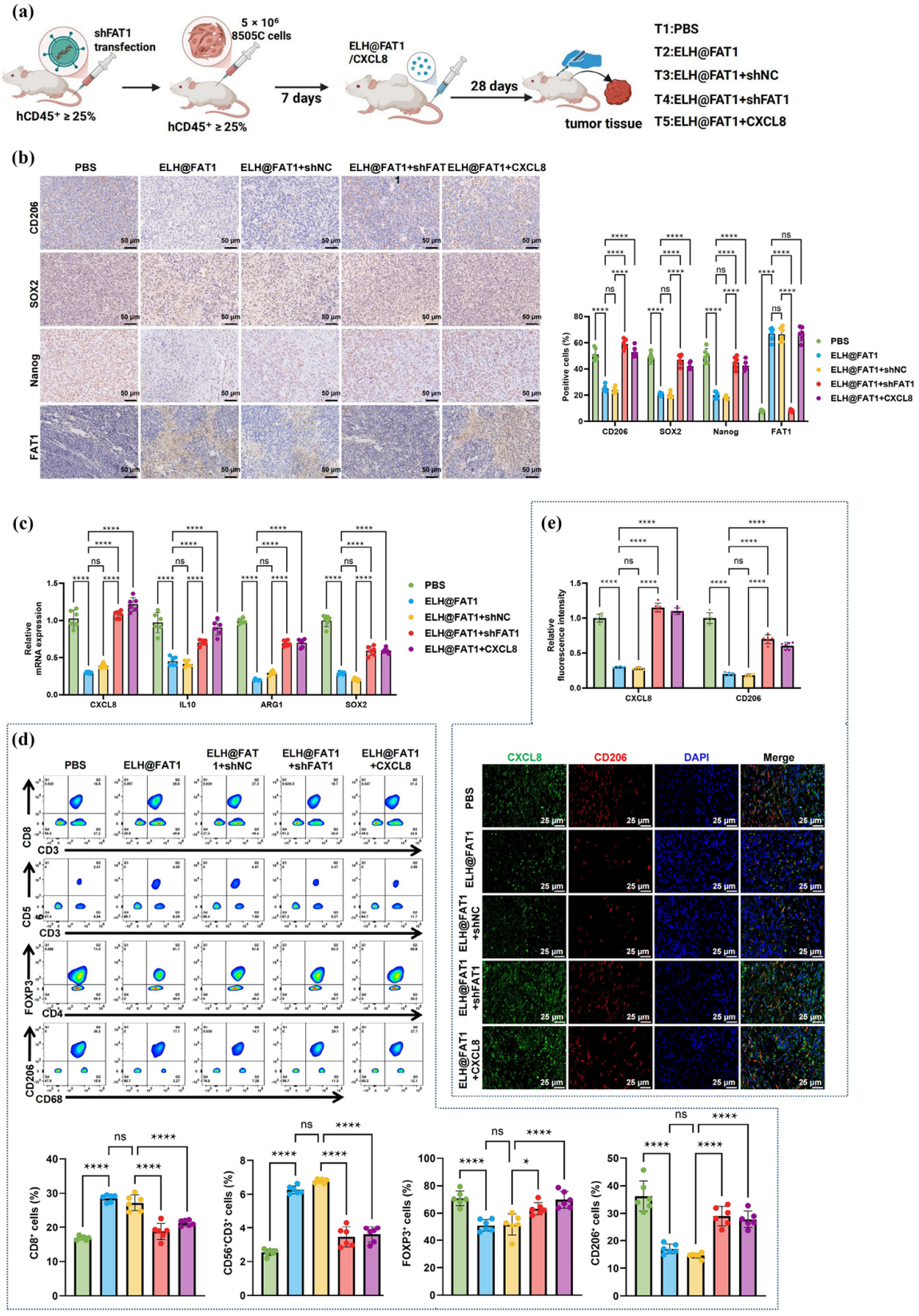

Figure 7 ELH@FAT1 upregulated FAT1 and disrupted the CXCL8-mediated stemness-immunity feedback loop. (a) Schematic workflow of the THCA xenograft model study investigating how ELH@FAT1 regulated immune-stemness interactions through CXCL8. (b) IHC staining of M2 TAM marker CD206, and stemness markers SOX2 and Nanog in tumor tissues (scale bars = 50 μm). (c) RT-qPCR analysis of CXCL8, ARG1, IL-10, and SOX2 mRNA levels in tumor tissues. (d) Multicolor flow cytometry analysis of the proportions of $CD8^+$ T cells, NK cells, Tregs, and M2 TAMs in tumor tissues. (e) Immunofluorescence double staining showing CXCL8 expression in $CD206^+$ TAMs (scale bars = 25 μm). Each group included six mice. ns indicates no significant difference between groups, ns, not significant, $^*P < 0.05$, $^{**}P < 0.01$, $^{***}P < 0.001$, $^{****}P < 0.0001$.

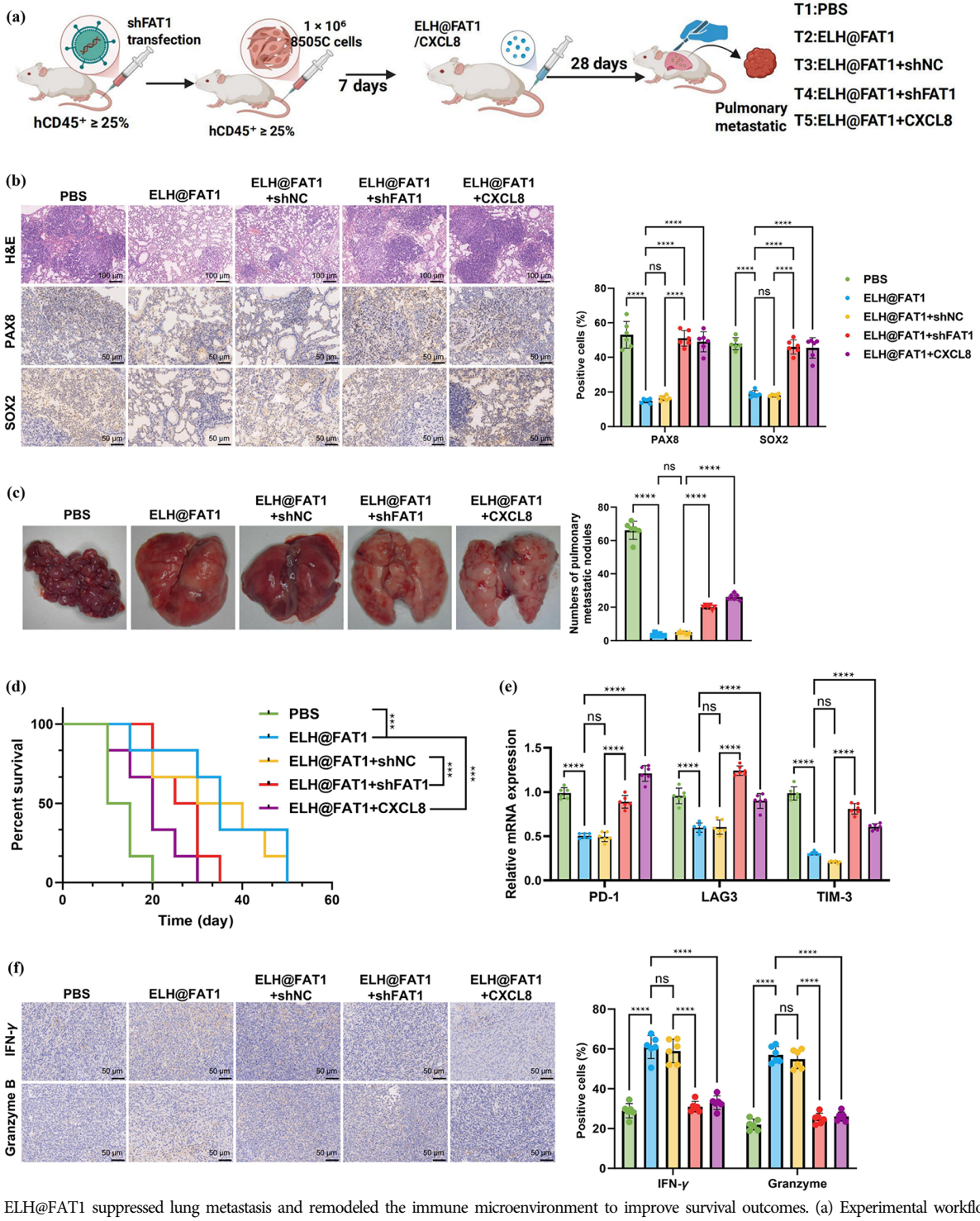

Figure 8 ELH@FAT1 suppressed lung metastasis and remodeled the immune microenvironment to improve survival outcomes. (a) Experimental workflow of the THCA lung metastasis model assessing ELH@FAT1-mediated regulation of immune-stemness interactions via CXCL8. (b) H&E and IHC staining of metastatic lesions in lung tissues and expression of stemness markers PAX8 and SOX2 (scale bars = 100 μm (top row 1)/50 μm (bottom 2 rows)). (c) Quantitative analysis of the number of metastatic nodules in lung tissues across groups. (d) Kaplan-Meier survival curves evaluating overall survival of mice in different groups. (e) RT-qPCR analysis of immune checkpoint molecules PD-1, LAG3, and TIM-3 in tumor tissues. (f) IHC staining of Granzyme B and IFN-γ expression in tumor tissues (scale bars = 50 μm). Each group included six mice. ns indicates no significant difference between groups, ns, not significant, $^{***}P < 0.001$, $^{****}P < 0.0001$.

macrophage M2 polarization and CXCL8 secretion. These two pathways often act in a coordinated manner: NF-κB drives the expression of pro-inflammatory and immunomodulatory mediators, whereas STAT3, in certain contexts, promotes immunosuppressive signaling and facilitates the M2 phenotype. Meanwhile, both pathways can converge to induce the expression of chemokines such as CXCL8, which subsequently regulates macrophage chemotaxis and polarization through receptors including CXCR1/2. Importantly, this process is highly dependent on tumor type and the composition of the TME, and is more likely

governed by a multi-pathway coupled network rather than a single linear causal axis [34–36]. Our findings support the role of FAT1 in downregulating CXCL8 expression and, for the first time, place FAT1 within the regulatory network of immune chemokine expression, highlighting its broader immunomodulatory potential. This discovery not only provides an entry point for further investigation of upstream regulators of FAT1 but also adds a new dimension to understanding the control of inflammatory pathways within the TME.

Regarding delivery strategy, this study developed an ELH@FAT1 nanoplatform, combining the targeting capacity of EVs with the structural stability of LNPs. Compared with conventional cationic LNPs or single EV carriers, this hybrid system exhibited superior *in vivo* biodistribution, enhanced mRNA protection, and improved cellular penetration. Structural stability was confirmed through TEM, FRET, and WB analysis, while functional validation demonstrated that the system exhibits high delivery efficiency in THCA cells. Collectively, these results indicate that ELH@FAT1 represents a delivery strategy better adapted to the complex and immunosuppressive microenvironment of solid tumors, highlighting its strong translational potential for mRNA-based cancer therapeutics.

scRNA-seq, as a powerful tool for dissecting TME heterogeneity, was employed in this study to track changes in immune cell interaction networks following ELH@FAT1 intervention. The results showed a marked reduction in $CXCL8^+$ M2-type TAM clusters, accompanied by enhanced T-cell activation, antigen presentation, and proinflammatory factor expression, indicating a shift in the TME from an immunosuppressive to an immune-activated state. Compared with bulk sequencing, single-cell data provided more direct evidence that FAT1 intervention possesses the capacity to "deconstruct and reconstruct" the tumor immune ecosystem. This study also demonstrated the potential of mRNA therapeutics in regulating intercellular interactions, thereby advancing mechanistic research to a deeper level. It should be noted that the sample size of single-cell sequencing in this study was relatively limited and may not fully capture inter-individual heterogeneity within the TME. In addition, interaction inferences involving low-abundance cell populations may have been constrained by sequencing depth. Nevertheless, it is important to emphasize that the key alterations identified by single-cell analyses were independently validated through multiple batches of *in vivo* and *in vitro* experiments, supporting the overall robustness of the proposed mechanistic conclusions. In future studies, we will increase the number of biological replicates for single-cell sequencing to achieve greater statistical power and confidence.

This work provides the first evidence that tumor stemness and immune evasion can be co-regulated through a single, unified signaling axis. Restoration of FAT1 expression not only suppressed EMT and stemness maintenance but also simultaneously reduced CXCL8-mediated immune evasion, thereby producing a "dual-intervention" therapeutic effect. This mechanism challenges the conventional paradigm that treats tumor stemness and immune escape as independent processes and instead establishes a conceptual framework in which both malignant features are functionally intertwined. By targeting the immune stemness feedback loop, this strategy has the potential to simultaneously enhance antitumor immune responses and weaken the intrinsic immune resistance of tumor stem cells, thereby improving responsiveness to immunotherapy.

Moreover, the FAT1/CXCL8 axis emerged as a promising target for combination immunotherapy. Currently, the efficacy of PD-1/PD-L1 inhibitors in some THCA patients is limited, likely due to the highly immunosuppressive TME. The mechanism uncovered in this study suggests that ELH@FAT1 could serve as a priming strategy for TME remodeling, with the potential to synergize with immune checkpoint inhibitors or CXCL8 receptor antagonists to amplify antitumor immunity. This approach provides a feasible pathway for constructing personalized, multi-targeted immunotherapeutic regimens and lays the groundwork for subsequent preclinical studies on efficacy and safety.

In summary, this study established an innovative FAT1 mRNA nanodelivery platform and demonstrated that it suppressed the polarization and secretion of $CXCL8^+$ M2-type TAMs, thereby disrupting the immune stemness feedback loop between TAMs and TSCs. Through this coordinated intervention, ELH@FAT1 simultaneously inhibits tumor stemness maintenance and metastatic progression, remodels the immunosuppressive TME, and improves therapeutic outcomes in THCA. By integrating nanotechnology, single-cell analysis, and immune-stemness mechanistic dissection, this work provides the first systematic evidence supporting FAT1 as an immunoregulatory target and highlights a novel conceptual and technological direction for mRNA-based precision therapy in solid tumors. For instance, the Western blot-based evidence supporting vesicle material fusion was not sufficiently comprehensive. Moreover, the mechanistic link by which increased FAT1 expression leads to CXCL8 downregulation remains unclear, including the specific tumor cell-derived pathways through which macrophage signaling programs (such as NF-κB or STAT3) are modulated. In addition, how the reduction of CXCL8 expression and the reprogramming of M2 macrophages subsequently influence tumor cell behavior has yet to be elucidated. The duration of the animal experiments was relatively short, and validation of clinical relevance requires further expansion. Furthermore, the number of animals used for single-cell sequencing analyses was limited; multiple-animal replicates should be incorporated to minimize confounding effects of inter-individual variability and to improve statistical inference. Future studies should focus on systematically dissecting the FAT1 signaling network, validating its biomarker potential in large clinical cohorts, and increasing the number of animals included in single-cell sequencing analyses. These efforts will help facilitate the translational development of FAT1-based therapeutic strategies, particularly in combination with immune checkpoint inhibitors or CXCR1/2 antagonists, toward clinical application.

5 Conclusions

This study systematically revealed that the loss of FAT1 expression in THCA plays a pivotal role in maintaining tumor stemness and fostering an immunosuppressive microenvironment. We constructed and validated the ELH@FAT1 nanosystem, which efficiently delivered FAT1 mRNA and reprogrammed the tumor stemness-immune interaction pathway. FAT1 upregulation suppressed the polarization of $CXCL8^+$ M2-type TAMs, disrupted the CXCL8-mediated TAM-TSC feedback loop, enhanced T cell effector functions, inhibited tumor growth and distant metastasis, and prolonged survival. For the first time, this work established an mRNA delivery nanosystem targeting FAT1 and elucidated the mechanism by which FAT1 regulates tumor stemness and the

immune microenvironment through the CXCL8 axis, thereby providing a new perspective on TAM–TSC interactions. The nanosystem exhibited favorable delivery efficiency and biocompatibility, highlighting its translational potential for immunotherapy in "cold tumors" such as THCA. This study primarily focused on the immunoregulatory role of the FAT1-CXCL8 pathway, without further addressing FAT1 functions in tumor metabolism or other immune cell subsets. Future investigations should integrate multi-omics, organoid models, and clinical samples to validate the adaptability and translational potential of FAT1 across multiple cancer types, thereby offering broader support for precision immunotherapy.

Electronic Supplementary Material: Supplementary material (additional experimental data for extracellular vesicle characterization (TEM, NTA, and Western blot analyses), physicochemical characterization and stability evaluation of the ELH@FAT1 nanosystem, TCGA bioinformatics analysis, *in vivo* biosafety assessment, detailed antibody information used for Western blot analysis (Table S1), and primer sequences used for RT-qPCR assays (Table S2)) is available in the online version of this article at https://doi.org/10.26599/NR.2026.94908637.

Data availability

All data generated or analyzed during this study are included in this article and its supplementary material files. Further enquiries can be directed to the corresponding author.

Acknowledgements

None.

Declaration of competing interest

The authors declare no conflict of interest.

Author contribution statement

W. J. W., J. Z., B. R. T., N. K., and J. S. conceived and designed the study. W. J. W., J. Z., and B. R. T. performed the experiments. N. K. and J. S. analyzed the data. W. J. W., J. Z., and B. R. T. wrote the manuscript. All authors reviewed and approved the final version of the manuscript.

Informed consent

Not applicable.

Ethics statement

All experimental protocols were reviewed and approved by the Animal Ethics Committee of Huashan Hospital (approval number: 2024-HSYY-308).

Use of AI statement

None.

References

[1] Boucai, L.; Zafereo, M.; Cabanillas, M. E. Thyroid cancer: A review. *JAMA* **2024**, *331*, 425–435.

[2] Zhu, L. Y.; Li, X. J.; Gangadaran, P.; Jing, X. L.; Ahn, B. C. Tumor-associated macrophages as a potential therapeutic target in thyroid cancers. *Cancer Immunol. Immunother.* **2023**, *72*, 3895–3917.

[3] Kimura, T.; Kruhlak, M.; Zhao, L.; Hwang, E.; Fozzatti, L.; Cheng, S. Y. Combinatory actions of cytokines induce M2-like macrophages in anaplastic thyroid cancer. *Am. J. Cancer Res.* **2024**, *14*, 5812–5825.

[4] Liu, Q.; Sun, W.; Zhang, H. Roles and new insights of macrophages in the tumor microenvironment of thyroid cancer. *Front. Pharmacol.* **2022**, *13*, 875384.

[5] Lv, J.; Liu, C.; Chen, F. K.; Feng, Z. P.; Jia, L.; Liu, P. J.; Yang, Z. X.; Hou, F.; Deng, Z. Y. M2-like tumour-associated macrophage-secreted IGF promotes thyroid cancer stemness and metastasis by activating the PI3K/AKT/mTOR pathway. *Mol. Med. Rep.* **2021**, *24*, 604.

[6] Turlej, E.; Domaradzka, A.; Radzka, J.; Drulis-Fajdasz, D.; Kulbacka, J.; Gizak, A. Cross-talk between cancer and its cellular environment-A role in cancer progression. *Cells* **2025**, *14*, 403.

[7] Grassi, E. S.; Ghiandai, V.; Persani, L. Thyroid cancer stem-like cells: From microenvironmental niches to therapeutic strategies. *J. Clin. Med.* **2021**, *10*, 1455.

[8] Yuan, W.; Zhang, Q.; Gu, D. L.; Lu, C. F.; Dixit, D.; Gimple, R. C.; Gao, Y. S.; Gao, J. C.; Li, D. Q.; Shan, D. Y. et al. Dual role of CXCL8 in maintaining the mesenchymal state of glioblastoma stem cells and M2-like tumor-associated macrophages. *Clin. Cancer Res.* **2023**, *29*, 3779–3792.

[9] Luo, S. H.; Yang, G. H.; Ye, P.; Cao, N. Q.; Chi, X. X.; Yang, W. H.; Yan, X. W. Macrophages are a double-edged sword: Molecular crosstalk between tumor-associated macrophages and cancer stem cells. *Biomolecules* **2022**, *12*, 850.

[10] Singer, M.; Zhang, Z. L.; Dayyani, F.; Zhang, Z. G.; Yaghmai, V.; Choi, A.; Valerin, J.; Imagawa, D.; Abi-Jaoudeh, N. Modulation of tumor-associated macrophages to overcome immune suppression in the hepatocellular carcinoma microenvironment. *Cancers* **2024**, *17*, 66.

[11] Xu, C. C.; Chen, J. Y.; Tan, M.; Tan, Q. Q. The role of macrophage polarization in ovarian cancer: From molecular mechanism to therapeutic potentials. *Front. Immunol.* **2025**, *16*, 1543096.

[12] Long, X. X.; Ye, Y. N.; Zhang, L. J.; Liu, P. P.; Yu, W. W.; Wei, F.; Ren, X. B.; Yu, J. P. IL-8, a novel messenger to cross-link inflammation and tumor EMT via autocrine and paracrine pathways (review). *Int. J. Oncol.* **2016**, *48*, 5–12.

[13] Fousek, K.; Horn, L. A.; Palena, C. Interleukin-8: A chemokine at the intersection of cancer plasticity, angiogenesis, and immune suppression. *Pharmacol. Ther.* **2021**, *219*, 107692.

[14] Chen, Z. G.; Saba, N. F.; Teng, Y. The diverse functions of FAT1 in cancer progression: Good, bad, or ugly. *J. Exp. Clin. Cancer Res.* **2022**, *41*, 248.

[15] Wang, T.; Li, J. T.; Du, J.; Zhou, W.; Lu, G. Recent advances in the role of atypical cadherin FAT1 in tumorigenesis (review). *Oncol. Lett.* **2025**, *29*, 110.

[16] Pastushenko, I.; Mauri, F.; Song, Y.; de Cock, F.; Meeusen, B.; Swedlund, B.; Impens, F.; Van Haver, D.; Opitz, M.; Thery, M. et al. *Fat1* deletion promotes hybrid EMT state, tumour stemness and metastasis. *Nature* **2021**, *589*, 448–455.

[17] Peng, Z. Z.; Gong, Y. Y.; Liang, X. Q. Role of FAT1 in health and disease (review). *Oncol. Lett.* **2021**, *21*, 398.

[18] Wang, Z. Y.; Lin, K.; Xiao, H. A pan-cancer analysis of the FAT1 in human tumors. *Sci. Rep.* **2022**, *12*, 21598.

[19] Srivastava, C.; Irshad, K.; Gupta, Y.; Sarkar, C.; Suri, A.; Chattopadhyay, P.; Sinha, S.; Chosdol, K. NFκB is a critical transcriptional regulator of atypical cadherin FAT1 in glioma. *BMC Cancer* **2020**, *20*, 62.

[20] Xu, S. Q.; Yang, K. P.; Li, R.; Zhang, L. mRNA vaccine era-Mechanisms, drug platform and clinical prospection. *Int. J. Mol. Sci.* **2020**, *21*, 6582.

[21] Dilliard, S. A.; Cheng, Q.; Siegwart, D. J. On the mechanism of tissue-specific mRNA delivery by selective organ targeting nanoparticles. *Proc. Natl. Acad. Sci. USA* **2021**, *118*, e2109256118.

[22] Arora, M.; Kundu, A.; Sinha, S.; Chosdol, K. Immune factors and their role in tumor aggressiveness in glioblastoma: Atypical cadherin FAT1 as a promising target for combating immune evasion. *Cell Mol. Biol. Lett.* **2025**, *30*, 89.

[23] Irshad, K.; Srivastava, C.; Malik, N.; Arora, M.; Gupta, Y.; Goswami, S.; Sarkar, C.; Suri, V.; Mahajan, S.; Gupta, D. K. et al. Upregulation of atypical cadherin FAT1 promotes an immunosuppressive tumor microenvironment via TGF-β. *Front. Immunol.* **2022**, *13*, 813888.

[24] Dikshit, B.; Irshad, K.; Madan, E.; Aggarwal, N.; Sarkar, C.; Chandra, P. S.; Gupta, D. K.; Chattopadhyay, P.; Sinha, S.; Chosdol, K. *FAT1* acts as an upstream regulator of oncogenic and inflammatory pathways, via PDCD4, in glioma cells. *Oncogene* **2013**, *32*, 3798–3808.

[25] Ha, H.; Debnath, B.; Neamati, N. Role of the CXCL8-CXCR1/2 axis in cancer and inflammatory diseases. *Theranostics* **2017**, *7*, 1543–1588.

[26] Xie, H. Y.; Yao, J.; Wang, Y. X.; Ni, B. Exosome-transmitted circVMP1 facilitates the progression and cisplatin resistance of non-small cell lung cancer by targeting miR-524-5p-METTL3/SOX2 axis. *Drug Deliv.* **2022**, *29*, 1257–1271.

[27] Zhang, L. S.; Gaskins, K.; Yu, Z. Y.; Xiong, Y.; Merino, M. J.; Kebebew, E. An *in vivo* mouse model of metastatic human thyroid cancer. *Thyroid.* **2014**, *24*, 695–704.

[28] Ning, J. Y.; Hou, X. K.; Hao, J.; Zhang, W.; Shi, Y.; Huang, Y.; Ruan, X. H.; Zheng, X. Q.; Gao, M. METTL3 inhibition induced by M2 macrophage-derived extracellular vesicles drives anti-PD-1 therapy resistance via m6A-CD70-mediated immune suppression in thyroid cancer. *Cell Death Differ.* **2023**, *30*, 2265–2279.

[29] Nilubol, N.; Yuan, Z. Q.; Paciotti, G. F.; Tamarkin, L.; Sanchez, C.; Gaskins, K.; Freedman, E. M.; Cao, S. G.; Zhao, J. L.; Kingston, D. G. I. et al. Novel dual-action targeted nanomedicine in mice with metastatic thyroid cancer and pancreatic neuroendocrine tumors. *J. Natl. Cancer Inst.* **2018**, *110*, 1019–1029.

[30] Fang, W. Y.; Ye, L.; Shen, L. Y.; Cai, J.; Huang, F. J.; Wei, Q.; Fei, X. C.; Chen, X.; Guan, H. X.; Wang, W. Q. et al. Tumor-associated macrophages promote the metastatic potential of thyroid papillary cancer by releasing CXCL8. *Carcinogenesis* **2014**, *35*, 1780–1787.

[31] Shao, J.; Wang, W. J.; Tao, B. R.; Cai, Z. H.; Li, H. X.; Chen, J. H. Extracellular vesicle-carried GTF2I from mesenchymal stem cells promotes the expression of tumor-suppressive FAT1 and inhibits stemness maintenance in thyroid carcinoma. *Front. Med.* **2023**, *17*, 1186–1203.

[32] Shao, Y.; Lan, Y.; Chai, X. Y.; Gao, S. H.; Zheng, J. X.; Huang, R.; Shi, Y.; Xiang, Y.; Guo, H. M.; Xi, Y. F. et al. CXCL8 induces M2 macrophage polarization and inhibits CD^{8+} T cell infiltration to generate an immunosuppressive microenvironment in colorectal cancer. *FASEB J.* **2023**, *37*, e23173.

[33] Šekoranja, D.; Zupan, A.; Mavčič, B.; Martinčič, D.; Salapura, V.; Snoj, Ž.; Limpel Novak, A. K.; Pižem, J. Novel *ASAP1-USP6, FAT1-USP6, SAR1A-USP6*, and *TNC-USP6* fusions in primary aneurysmal bone cyst. *Genes Chromosomes Cancer* **2020**, *59*, 357–365.

[34] Grivennikov, S. I.; Karin, M. Dangerous liaisons: STAT3 and NF-κB collaboration and crosstalk in cancer. *Cytokine Growth Factor Rev.* **2010**, *21*, 11–19.

[35] Cao, Y. N.; Yi, Y. A.; Han, C. X.; Shi, B. W. NF-κB signaling pathway in tumor microenvironment. *Front. Immunol.* **2024**, *15*, 1476030.

[36] Lee, H.; Herrmann, A.; Deng, J. H.; Kujawski, M.; Niu, G. L.; Li, Z. W.; Forman, S.; Jove, R.; Pardoll, D. M.; Yu, H. Persistently activated Stat3 maintains constitutive NF-κB activity in tumors. *Cancer Cell* **2009**, *15*, 283–293.